Formation of the Circumgalactic Medium in Cosmological Zoom-in Simulations

Isak Lindh

Division of Astrophysics
Department of Physics

LUND UNIVERSITY

2026–EXA264

Degree project of 60 higher education credits
June 2026

Supervisors: Oscar Agertz & Santi Roca-Fàbrega

Division of Astrophysics
Department of Physics
Box 118
SE-221 00 Lund
Sweden

Abstract

The gaseous halo around galaxies, known as the circumgalactic medium (CGM), has been inferred from observations and simulations to transition from cold chaos to hot stability (virialisation), but the road it takes is uncertain. One of the possible routes is via the ejections of energy and matter from stars, called stellar feedback, within the galaxy, providing the necessary thermal support to stabilise the CGM. In this thesis, the evolution of the CGM was analysed and compared between multiple state-of-the-art simulations provided by the AGORA Collaboration. These simulations varied primarily in their numerical implementation and stellar feedback model. By matching their gas properties, each simulation could be distinguished in their CGM by their unique set of assumptions, and an improved understanding of their respective models and implementations could be gleaned. Each code predicted a CGM baryon mass fraction relative to the cosmic baryon fraction in the range of $\sim 20-50\%$, implying all could regulate and maintain a significant fraction of baryons from their central galaxy in the CGM, albeit with different efficiency. The thermal phases of these baryons varied significantly, where certain codes with strong preventive feedback developed a hot gas dominated CGM early at $z \gtrsim 4$, before predicted accretion shocks, while some with instead strong ejective feedback predicted a much later transition at $z \lesssim 1.5$. It was shown that including kinetic feedback, together with thermal, also greatly improved the ability to eject baryons, improving the regulation of the total baryon fraction. An odd commonality between most codes, independent of their numerical implementation or stellar feedback model, was a shared tendency towards halo wide virialisation, at similar times in the outer regions. This does not align with the current standard theories that predict a stronger radial dependence for the virialisation, either stabilising from the inside-out or from the outside-in, and therefore has interesting implications for the evolution of the CGM.

Contents

Acknowledgements

First and foremost, I want to thank my fantastic supervisors Oscar Agertz and Santi Roca-Fàbrega for their immeasurable guidance not only in this project and the paper herein, but also in navigating the chaotic world of academia. This thanks also extends to my honorary third supervisor Víctor Rufo-Pastor, whose assistance for this period has been incredibly meaningful. I also want to thank the rest of my fellow galaxy group members for their support and sympathy. I am also incredibly grateful for my fellow master students, many of which I now call dear friends, for the very welcome distractions that have kept my sanity in check. Finally, I extend my sincere thanks to the programme coordinator Jens Hoeijmakers, and my examiners Ross Church and Brian Thorsbro.

Popular Science Summary

If the Universe is the Earth, then galaxies are its biomes. Like the rainforests and the savannas, galaxies also have ecosystems, although not primarily made from organisms but rather a long series of complicated and extreme interactions covering almost every field of physics. A critical component of any ecosystem is the atmosphere and in the galactic context, the atmosphere is represented by a vast gaseous halo called the circumgalactic medium, henceforth the CGM. The CGM acts as the interface between the central galaxy, called the interstellar medium (ISM), and the outside environment, named the intergalactic medium (IGM). The primary purpose of the CGM is to facilitate and mediate the circulation of gas, called the baryon cycle, via the inflows from the IGM and outflows from the ISM. Gas is the primary fuel for galaxies because from it, given the right conditions, stars can be born. But its ability to allow gas to pass is determined by its stability. First it will be unstable, meaning the gas that flows through it can pass with little hindrance. In this scenario, the galaxy will consume as much of the surrounding gas as it can, but will also easily lose gas from e.g. its stars ejecting energy, matter, and momentum as they evolve via e.g. supernovae. You can think of this as a typical teenager who just got their first job, a lot of money coming in but also no sense of saving. This is a chaotic time and not sustainable, and, for galaxies, does not promote long lived structures, such as disks. If the CGM is instead heated enough, matured, it can provide a sufficient and stable thermal support, acting as a pressure, that will impede gas flows. In this state, it would be considered virialised, and gas can be stored inside the CGM for a longer time and instead slowly fed into the galaxy in an inner region of semi-stability.

How the CGM reaches this hot, virialised state is currently up for debate. Some models predict that it naturally occurs when the galaxy grows massive enough for the infalling gas to be gravitationally accelerated to supersonic velocities. When this gas encounters the medium inside the CGM, like a jet plane through the sky, a sonic boom, or in this case just a shock wave will form. Along these waves' journey, they transfer heat into the surrounding gas, which in turn supports them from behind with a thermal pressure, and as they travel throughout the CGM they provide the necessary temperature for stability. But recent observations reveal that this approach might be too slow. This work explored the alternative, or possibly complimentary, route where the stars from within the galaxy might be able to provide the needed thermal energy for the CGM to stabilise much earlier. As stars age, they eventually evolve depending on their mass, and the result of this evolution is often violent which ejects significant energy and gas into their surroundings, called stellar feedback, or in this work just feedback. But due to current limited observational capabilities, especially for galaxies like our own Milky Way, we must test our theories via simulations. In order to do this, we must ensure that the simulations we construct and the physics they include are robust, which is the aim of this project and the involved AGORA Collaboration. A lot of detail goes into these simulations, and due to the very fickle nature of simulations (think butterfly effect), we must first run them before we can see the effects of our chosen assumptions. By comparing the CGM evolution in simulated galaxies like our own Milky Way from using different implementations and different models for the stellar feedback, this work showed that we can reverse engineer galaxies like our own and learn more about which assumptions result to what. Specifically, by analysing and matching the distributions of gas properties in both space and time inside the CGM, this work managed to link the resulting evolution and formation of the galaxies to their respective assumptions. This is one of the many stepping stones on a long journey towards understanding how galaxies, like our own, form and evolve.

Chapter 1

Introduction

We can find much of ourselves in galaxies, they too could not survive alone, they too rely on the nurturing of their surroundings. Just like us humans, we can not explain the origins of galaxies' many complex characteristics today by just observing them as they are, we have to understand where they came from. But unlike us, they are not here on Earth (or in its orbit), and so to study them or their past requires significant effort and approximations. Generally though, these methods and considerations can be grouped up based on three different approaches: observational, what we can see; theoretical, what we can consider; and numerical, what we can recreate, but they each work best together.

This work aimed to analyse and compare several numerical simulations, each with different numerical implementations and theoretical models, in order to test the validity and self-consistency of our current understanding of certain physical processes that allow for the evolution of galaxies. To do this, eight state-of-the-art Milky Way-mass[1] simulations were considered. Each simulation used the same initial conditions, heating/cooling method, and star formation thresholds, but with different numerical approaches and treatment of stars effect on their surroundings, i.e. stellar feedback. They were all run by members of the AGORA Collaboration (see the AGORA Paper III and IV Roca-Fàbrega et al., 2021, 2024). By then comparing these simulations and testing them with idealised models, the hope was to sift out results that align with our predictions, improving our understanding (e.g. Gronke & E. Schneider, 2026). This has been tried, and is possible, for many different aspects of galaxy formation and evolution, but one that currently a very promising candidate is the circumgalactic medium (CGM) (Tumlinson et al., 2017). The CGM acts as the galactic middleman that handles the exchange of gas between the intergalactic medium (IGM), the gas between galaxies, and the interstellar medium (ISM), the gas between stars within galaxies. This gaseous interchange, called the baryon cycle, is vital to sustain the formation of galaxies but its details and longevity relies strongly on the state and stability of the CGM, which is still not clear Wright et al. (2024). The main goal of this work was to analyse and compare the evolution of the CGM in several different cosmological simulations provided by the AGORA Collaboration (see Chapter 2). By applying the same theoretical model for the CGM stability, the details on how they establish their CGM differently depending on numerical implementation and stellar feedback model could be revealed. This is also done to strengthen their previously found both similarities and differences in past AGORA papers.

This project is structured as follows. This chapter (Chapter 1) continues onto the more in-depth context, both historical and theoretical, that is required moving forward. This includes first a quick overview of the standard cosmological model, in Section 1.1, i.e. the framework that all the simulations, models, and most of the theory that is in this work is based on; then in Section 1.2 there is a brief summary of the theory of galaxy formation; in Section 1.3 there is a more comprehensive guide to the CGM, including observational, theoretical, and numerical context; and in Section 1.4 contains a short motivation and historical introduction to the pursuit of simulation comparisons. Following this, in Chapter 2, the AGORA project and their method

[1] Milky Way-mass means similar current epoch halo mass of $M_{\rm h} \sim 10^{12}\ M_\odot$.

for code comparison is presented. The codes selected for this work are also introduced, together with their common physics but also their respective differences in terms of both physical and numerical considerations. Chapter 3 includes the common AGORA analysis tool `yt`; the specific assumptions used to define the CGM boundaries and its different gas phases; how the baryon cycle was analysed, including the definition for the baryon budget and closure radius; and finally the definitions for the cooling time and free-fall time used to define CGM stability. Chapter 4 contains the paper. Finally, Chapter 5 summarises the important takeaways and presents the conclusions that can be drawn from this project together with outlook for future work.

1.1 Cosmological Model

When considering the Universe, or a significant portion of it, e.g. for a simulation, one must first decide what it contains and how it develops, from its beginning onwards. The specific choice made is usually called the cosmological model, or just the cosmology, of the system. In this work, all cosmological simulations that were analysed assumed the same ΛCDM cosmology, often called the Standard Model of Cosmology. Generally, modern cosmological models contain three fundamental components:

- **The cosmological constant (Λ)**, connected with dark energy, a nebulous energy that permeates the Universe that is responsible for the acceleration of the expansion of space (e.g. Carfora & Familiari, 2026).
- **Dark matter**, which is the missing yet dominant source of matter ($\sim$ 85%) in the Universe, and many studies strongly motivate dark matter's existence, despite its non-detection (for a recent review see Cirelli et al. (2024)). Not only is its origin unknown, the nature of dark matter is also poorly constrained, where models usually change its assumed velocity depending on if its hot (high velocity), warm (intermediate velocity) or cold (low velocity) dictating its ability to interact and form structures. In the case of ΛCDM cosmology, the "CDM" stands for cold dark matter. While the source responsible for dark matter has not yet been confirmed, for the purposes of cosmological simulations this is not much of a problem. Dark matter can simply be thought of as some particle with a certain mean velocity, depending on the model, that only interacts gravitationally, and is conserved, i.e. it never converts/decays into other matter/energy.
- **Normal baryonic matter** includes protons, neutrons, and electrons[2] contained either in stars, dust or gas.

To describe the actual behaviour and development of the ΛCDM Universe, two main postulates are also included and assumed to hold:

- **The cosmological principle**, which is an assumption that at sufficiently large scales, the Universe is isotropic and homogeneous at every point in space. This means that if you observe sufficiently far away in any direction at any location, you will see the same general structure, i.e. nowhere is special[3].
- **General relativity**, and that the theorems contained within can determine the structure of spacetime using only the distribution of mass in the Universe.

These assumptions can be combined to define a cosmological model describing the behaviour of spacetime using only the curvature of the Universe k and the scale factor $a(t)$[4]. In the ΛCDM model, the curvature of the Universe can vary but in this work is assumed to be flat following observational evidence (e.g. Planck Collaboration et al., 2020). Flat in this context implies that the ratio between the total energy density ρ over the critical density ρ_{c}, $\Omega(t)$, at all times is equal to one. In the simulations used in this work, the contributions

[2] Note that electrons are not actually baryons but, like how we consider all elements heavier than helium to be metals in astronomy, we take the liberty of considering them baryonic in this context.
[3] In a cosmological sense generally true, but you may disagree with this.
[4] Which describes how the length scale of the Universe changes with time.

of baryonic matter was $\sim 4\%$, cold dark matter (CDM) was $\sim 23\%$, and dark energy was $\sim 73\%$, for more specific details regarding the common physics of the simulations see Section 2.1.1. For an overview picture of a ΛCDM Universe, see Figure 1.1.

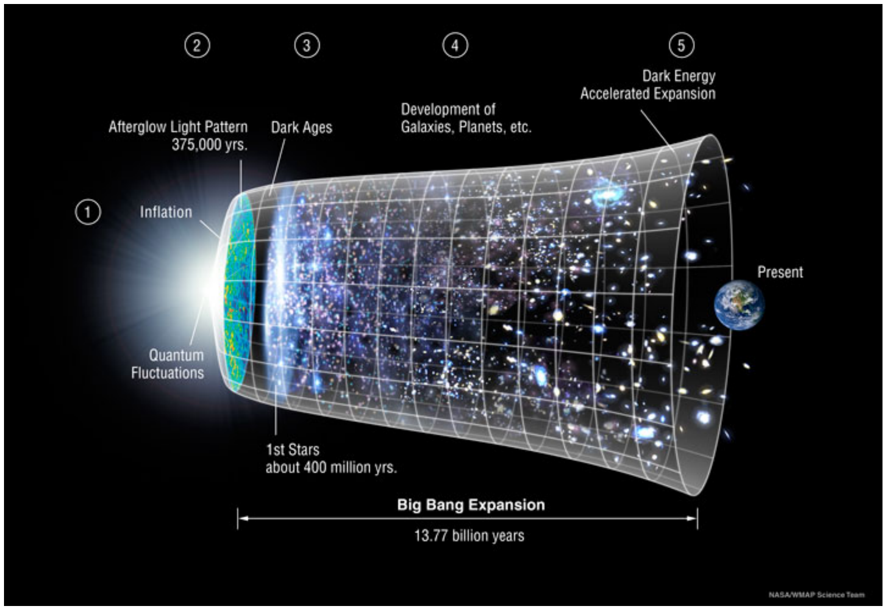

Figure 1.1: An approximate overview of the Universe assuming the ΛCDM cosmological model (NASA/LAMBDA-Science-Team, 2016).

1.2 Formation of Galaxies

The formation of galaxies in a ΛCDM Universe started with the gravitational collapse of dark matter in the very early Universe. This created dark matter concentrations, referred to as dark matter haloes, with higher than average density, and voids with less than average density (Mo et al., 2010). This was the origin of the so called cosmic web, a network of dark matter haloes linked together by filaments of matter both on small-scales, between galaxies, and large-scales, between galaxy groups and clusters.

In order to construct a galaxy, including gas, stars, dust etc., from this dark matter halo, it needs baryonic matter as well. The gas inside the cosmic web will feel a gravitational attraction to these dark matter haloes and be accreted, falling in to their central potential, through the CGM (see Section 1.3). As the gas is accreted, it will heat up from interactions with the surrounding medium but given efficient cooling, sufficiently dense, it will keep collapsing into cold and dense molecular clouds inside the ISM, which will subsequently collapse into stars. At this stage you have already have a galaxy, but depending on e.g. angular momentum and environmental interactions, the size and morphology can vary significantly, see Figure 1.2.

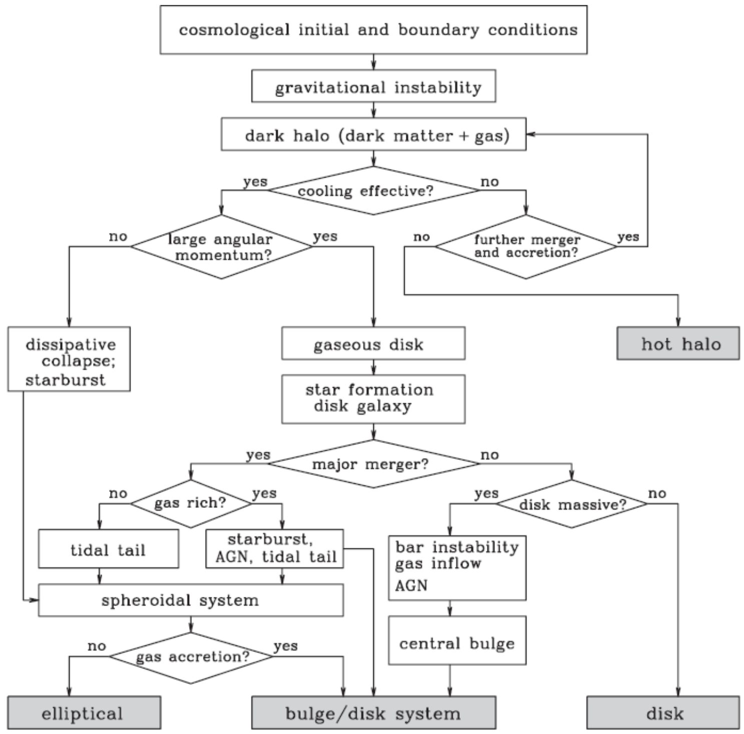

Figure 1.2: A flowchart following a simplified model of galaxy formation from Mo et al. (2010). Note that certain details have since been updated (see e.g. Naab & Ostriker, 2017), but it still functions as a useful guide for the basic steps of galaxy formation.

Galaxies are usually not formed in isolated regions and will have many neighbouring galaxies that have undergone or are undergoing a similar formation process[5]. If galaxies are close enough together, they may become gravitationally bound and eventually merge which, depending on the masses relative to each other, can cause a significant change in their properties. The ΛCDM model predicts that galaxies gain much of their mass and volume via mergers, hierarchically, which provides the explanation for the more massive galaxies that we observe.

The stellar population of the galaxy will age and then eventually evolve, earlier the more massive they are. This evolutionary step often returns some or all of the stars mass (including metals), momentum, and energy to their surroundings via e.g. supernovae explosions. These outgoing winds contribute to the overall outflows of the galaxy, ejecting gas, metals, and energy from the ISM into the CGM or beyond to the IGM (see Section 1.3). This is what is referred to as stellar feedback, or often just feedback due to the lack of any other considered sources of feedback, such as from active galactic nuclei (see e.g. Suresh et al., 2015).

1.3 The Circumgalactic Medium

One of the fundamental processes that occur in galaxies is star formation. The problem is that it is a costly and complicated endeavour and requires not only the right conditions, i.e. cold and dense via efficient cooling, but also vast amounts of available gas. As galaxies grow their stellar populations, using what resources (gas) they have collected in their ISM, their material will quickly be consumed, and star formation should cease far earlier than what we observe (e.g. Peeples et al., 2014).

[5]Although not exactly the same depending on their formation time, mass, angular momentum etc.

A promising answer to this discrepancy is simply that galaxies are not isolated island Universes, as once thought (Hubble, 1925). Instead, they are part of a vast and complex cosmic ecosystem, exchanging matter and energy with their surroundings, allowing them to grow far beyond their initial potential. The cosmic supplier of new or recycled matter is a vast gaseous envelope called the circumgalactic medium (CGM) and is the mediator between the ISM of the galaxy and the local IGM. Within this region, intricate and multi-scale physical processes take place, driving the in- and outflows of baryonic matter, the baryon cycle, see Figure 1.3 (Faucher-Giguère & Oh, 2023). The galaxies accrete gas from the local IGM, through the CGM, to the ISM and this gas will then fuel the internal processes such as star formation. But then as stars are born, they will over their lifetime return energy, momentum, and enriched matter (e.g. metals) back into the ISM in the form of stellar feedback, via e.g. supernovae explosions, radiation, and stellar winds. Depending on the intensity of this injection, this feedback could drive the ejecta further, beyond the ISM and into the CGM. At this stage, this expelled material may be recycled back into the ISM, if the potential well of the galaxy is sufficient, otherwise it will escape the galaxy entirely and instead enrich the IGM. This means for intermediate and smaller galaxies of Milky Way-mass and less, stellar feedback is vital for the regulation of baryons (Fielding et al., 2017).

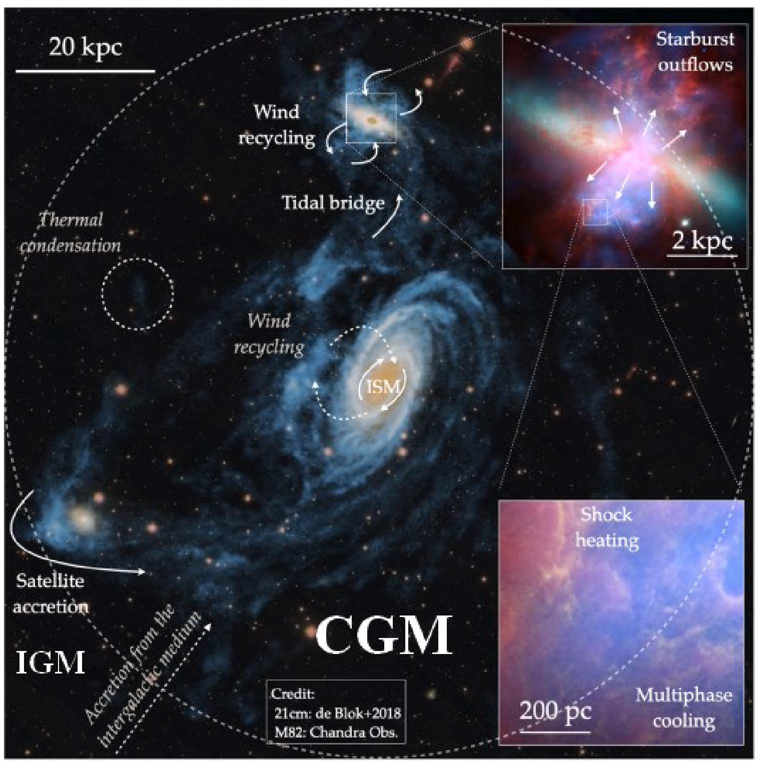

Figure 1.3: An illustrated overview of the CGM and some of many physical processes therein from Chen & Zahedy (2026).

Overall, it has been made clear that studying the CGM and its history is vital to understanding galaxy evolution, as it contains insights into the pivotal interactions and events responsible for the characteristics of galaxies and why they can look so different (Tumlinson et al., 2017).

1.3.1 Observing the Circumgalactic Medium

In order to understand, or at least constrain, the CGM, one must observe it. The presence of a hot corona, that later became the CGM, was first mentioned in Spitzer (1956), while later being properly analysed in (Münch & Zirin, 1961). Observations were done via absorption lines along the line of sight of hot stars in our own Milky Way and these lines were evidence for cold, dense clouds whose existence hinted towards a hot and diffuse gaseous corona that must surround our galaxy.

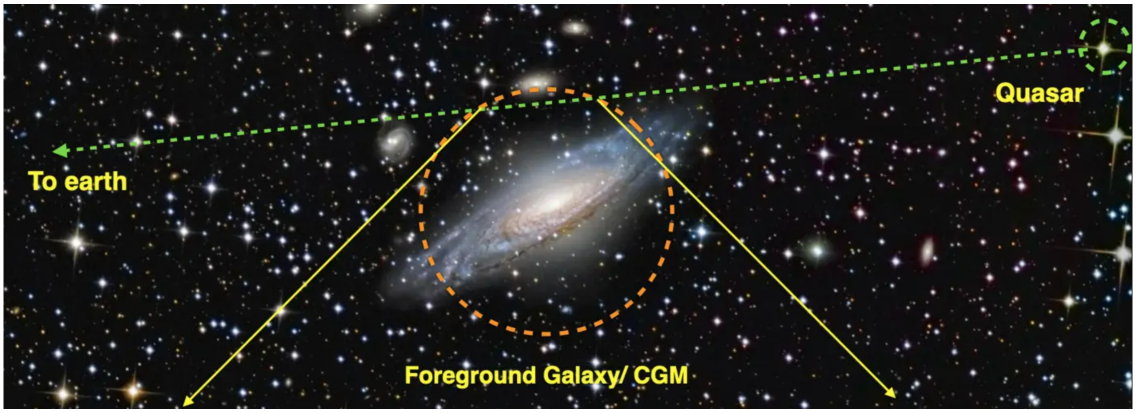

Figure 1.4: An example schematic of absorption line spectroscopy for observing the CGM via a background quasar (Credit MPA, Anand et al., 2021)

Using background sources to investigate the CGM via absorption line spectroscopy is still a very active observational method, but the modern alternative to hot stars is instead quasars (see Figure 1.4) (e.g. Rauch, 1998; Wolfe et al., 2005; Ng et al., 2025). The emitted photons will travel from the background source, through the diffuse medium of interest, creating distinguishable absorption lines in the spectra of the beam before it is detected by us, either on Earth or by a space telescope, such as the Hubble Space Telescope. The observational strength of these lines depends on the e.g. density, temperature, ionization state, and metallicity of the gaseous medium, which is invaluable for the multiphase CGM, see Section 1.3.2. A major issue with this method, however, is that it relies on the rare chance alignment of a quasar along the line of sight with the CGM of a galaxy, which if it is observed generally only happens once per galaxy-quasar pair. This means that these observations are kept at a high uncertainty, due to the lack of repeatable observations of the same system, and studies rely on statistically sampling multiple similar galaxy observations, losing their unique characteristics (e.g. Zhu & Ménard, 2013).

The other major observational method is directly via the faint emission of the gas. This method instead offers a 3-dimensional view of the galaxy structure, as it does not rely on a line of sight background source (e.g. Peng et al., 2025). The main issue, however, is that the emission strength is not only dependent on the brightness of the galaxy, but it is also proportional to $n_{\rm H}^2(1+z)^{-4}$ (van de Voort & Schaye, 2013). The total $(1+z)^{-4}$ term arises due to the expansion of our Universe via the combination of varying consequences: one term is from stretching the wavelength, decreasing the photon energy; another from time-dilation, stretching out the arrival time of the photons; and finally two from the angular area of the target being magnified and the energy is smeared out across a larger surface (Tolman, 1930; Tolman, 1934). Individual observations of Milky Way-mass, and smaller, galaxies are thus only possible if they are nearby, greatly limiting surveys and studies to low-redshift systems, meaning after significant epochs of their formation. While it is possible to make statistical analyses by stacking smaller and higher redshift galaxies, they still come with great uncertainty and lose important physical insights (e.g. Zhang et al., 2024b).

Due to both of these observational methods being dependent on the gas density and ionization state means that larger galaxies, galaxy groups, and galaxy clusters are naturally easier to observe. On the other hand, the CGM belonging to intermediate galaxies, such as Milky Way-mass galaxies and smaller, are more difficult to observationally constrain. Generally only those closest to us, such as our own Milky Way, Andromeda etc., are observable. This highlights the complementary need for galaxy simulations, as they allow us to try and predict the behaviours of these galaxies in their early formation epochs based on the knowledge that we do have (Tumlinson et al., 2017).

1.3.1.1 Major Observational Problems

The fundamental objective in galaxy evolution and formation is to determine and explain why despite all galaxies forming from a seemingly simple origin they can be so vastly diverse across cosmic time. While there is currently many major problems all related to this primary goal, at least three of them are directly associated with the CGM, due to their relation to star formation and the baryon cycle (see Chen & Zahedy, 2026, for further details).

1. **Why are galaxies so inefficient at turning their baryons into stars?** Each galaxy has a cosmological budget of baryons equal to $\frac{\Omega_\mathrm{b}}{\Omega_\mathrm{m,0}} M_\mathrm{vir} \approx 0.8 - 3.5 \times 10^{11} M_\odot$ for Milky Way-mass galaxies (Zhang et al., 2026), where Ω_b is the baryonic matter fraction, $\Omega_\mathrm{m,0}$ is the present day matter fraction, and M_vir is the virial mass defined here as the total dark matter mass within the virial radius. What has been observed, however, is that galaxies, regardless of mass, only contain a small fraction of this budget in their stars and ISM gas. Even Milky Way-sized galaxies that seem to be most efficient at star formation, converting gas into stars, seems to only use less than 20% of their available baryonic budget to make stars. Less massive dark matter haloes, hosting dwarf galaxies have been found doing much worse, spending less than $\lesssim 5\% - 10\%$ of their baryonic budget (Kravtsov et al., 2018). Due to this apparent dependency between star formation efficiency and baryonic budget expenditure, searching for answers in the region which is believed to be responsible for regulating the gas used for star formation, the CGM, might provide with further insight into the physical processes affecting this discrepancy.

2. **Where are the missing baryons and how did they get there?** Considering now that the galaxy itself can not account for all the baryons, they must be somewhere else. There are, as of now, three possible answers to this. The first is that that the baryons could have been accreted into the dark matter haloes of galaxies but then, due to star formation activity and other possible sources of energetic feedback, they were ejected out from their halo. The second option is that the baryons are still inside the dark matter haloes but have not been detected yet due to being too hot/diffuse making observations difficult. The third, and perhaps the most simple answer, is that the baryons are still in the IGM, without ever being accreted, and some process is preventing them from falling into the dark matter haloes. Most likely all will be to some capacity correct but with different significance at different epochs. By studying the physical properties of the CGM, which acts as a record of past accretion/ejection, these three different possibilities can likely be unravelled.

3. **What causes the quenching of galaxies?** The CGM does not only fuel the ISM star formation via rapid cold accretion, see Section 1.3.3, it is also believed to be responsible for its end (Tumlinson et al., 2011). It has been observed that a surprising amount of massive galaxies, with $M_\mathrm{tot,star} \gtrsim 10^{10.5}$ $\mathrm{M}_\odot$ and $M_\mathrm{halo} \gtrsim 10^{13}$ $\mathrm{M}_\odot$, cease their active star formation, i.e. quench, much earlier than expected, some just two billion years after the Big Bang (Long et al., 2024). This does not align with our current cosmological models and understanding of the physical processes that cause quenching, and as the CGM is most likely the primary culprit, studying it might reveal why these galaxies can be quenched so quickly.

1.3.2 Multiphase System

The CGM has a complicated environment both in terms of dynamics but also due to gas naturally coexisting at different temperatures, densities, and ionization states both in simulations and observations (Peroux & Nelson, 2024). In observational terms, the CGM can be considered multiphase because the metal ions involved in the ionization structure span an order of magnitude in ionization potential energy while commonly found in the same spatial region inside the halo of a galaxy. Conventionally, the CGM can be divided up, based on the ionization energy used to detect them, into four different thermal phases:

- **Cold Phase** ($T < 10^4$ K): The gas belonging to this phase could have originated from clouds swept along in multiphase outflows, alternatively from initially heated gas that cooled due to thermal instability. The gas in this phase is traced by neutral and low-energy ions such as H I, Na I, Ca II, and dust. By tracing high velocity clouds (HVCs), Putman et al. (2012) could estimate the total cold gas mass in the Milky Way halo to be $M = 2.6 \times 10^7$ $M_\odot$. Combining this mass with that estimated from the Magellanic Stream ($\sim 3 \times 10^8$ $M_\odot$), total dust mass (at most $\sim 1\%$ of baryonic budget), and metals in the cold gas ($\lesssim 1\%$ of the baryon budget), the cold component will only contribute with a few percent of the baryon budget.

- **Cool Phase** ($T \sim 10^{4-5}$ K): Going up to slightly higher temperatures the gas is instead in the so called cool phase. This component has a plentiful supply of UV lines, meaning with the Cosmic Origins Spectrograph (COS) aboard the Hubble Space Telescope (HST), it could be very accurately constrained. By using photoionization modelling combined with tracing Lyman-α absorption and low/intermediate ions (mostly C II, C III, Si II, Si III, N II, and N III), the total cool CGM mass for Milky Way-size galaxies could be estimated, using different approaches, to $M_{\rm cool} = 6.5 \times 10^{10}$ $M_\odot$ by Werk et al. (2014), $M_{\rm cool} = 9.2 \pm 4.3 \times 10^{10}$ $M_\odot$ in Prochaska et al. (2017), and $M_{\rm cool} = 1.3 \pm 0.4 \times 10^{10}$ $M_\odot$ (conservative minimum) from Stern et al. (2016). Overall, it is clear that this thermal component of the CGM seems to contain a relatively significant fraction of the baryon budget.

- **Warm Phase** ($T \sim 10^{5-6}$ K): The warm component is not as well-defined as the other phases, as it can easily blend together with either the hot or cool phases. This makes sense considering that the observed warm (or sometimes hot-warm) phase gas is most likely a transient transitional phase between cold clumps and the hot corona, forming via shocks or turbulent mixing due to in/outflows interacting with the surroundings (Chen & Zahedy, 2026). This is particularly noticeable when tracing the high-energy ion O IV, because if it is partially photoionized then a significant fraction of the already included $T < 10^5$ K gas in the cool phase will be also included (Werk et al., 2016). However, by tracing O IV, several works have managed to produce an estimate on the total warm CGM mass in Milky Way-mass galaxies, such as $> 2 \times 10^9$ $M_\odot$ from Tumlinson et al. (2011), and $\frac{0.5 Z_\odot}{Z} \times 10^{9.5-9.8}$ $M_\odot$ in Qu & Bregman (2019). This shows that the warm component, despite being considered a transition phase between the hot and cool, contains a non-negligible fraction of the baryons.

- **Hot Phase** ($T > 10^6$ K): This phase consists of the gas that has reached the virial temperature $T_{\rm vir}$, which for dark matter haloes with masses $M_{\rm h} \gtrsim 10^{12}$ $M_\odot$ will be $T_{\rm vir} \gtrsim 10^6$ K. Unfortunately, due to the gas belonging to this phase being generally very diffuse it becomes very difficult to detect, especially for galaxies with stellar masses less than 3×10^{11} $M_\odot$ due to low surface brightness (Zhang et al., 2024a). Several attempts at estimating and constraining the total hot gas mass have been made, one such recent example is by Zhang et al. (2024a) where they got the hot CGM X-ray emission by stacking detected X-ray emissions, masking the detected X-ray point sources, and then modelling the unresolved X-ray emissions from active galactic nuclei (AGN) and X-ray binaries (XRB). From this they estimated the combined baryon fraction of the hot CGM gas mass plus the stellar mass for Milky Way-mass galaxies to be 0.12 ± 0.06. Comparing this to the estimated baryonic fraction of 0.16 and considering that the stellar contribution is fairly low for MW-mass galaxies implies that the hot corona most likely contains a very significant amount of the baryonic budget.

1.3.3 Gas Flows and Virialisation

While there are many key cosmological processes that control and shape the CGM, such as satellite galaxies and angular momentum, the focus of this work is on the in- and outflows that occur between the IGM, CGM, and ISM (Faucher-Giguère & Oh, 2023). In order to simplify the highly complex CGM, the gas cooling physics can be approximated with spherical symmetry and no feedback (Birnboim & Dekel, 2003). In this idealised system, gas being accreted onto more massive dark matter haloes, such as Milky Way-mass of $\sim 10^{12}$ $M_\odot$, will reach supersonic velocities. As this inflowing gas passes through the galactic medium, it will be shock-heated to a temperature close to the virial temperature of the dark matter halo (defined in Section 3.2). The fate of this shocked gas depends on three different timescales (Dekel & Birnboim, 2006):

- The Hubble time $t_\mathrm{H} = 1/H(z)$: The typical cosmic time scale, defined using the redshift-dependent Hubble parameter $H(z)$.
- The free-fall time t_ff (see Section 3.3.1) : Is the time for a zero pressure, homogeneous sphere with some radius and mass to gravitationally collapse.
- The cooling time t_cool (see Section 3.3.1) : The time it takes for a volume of gas to radiate away all of its internal energy.

Using these timescales, two different modes of gas accretion can be considered:

- **Cold accretion** : Occurs when $t_\mathrm{cool} < t_\mathrm{ff}$, i.e. when the shock-heated gas cools faster than the time it takes to establish thermal equilibrium and thus the gas will lose its pressure support. Without thermal pressure support, gas will start fragmenting and form clumps or narrow filaments referred to here as "cold flows", but have also been called "cold streams". These cold and dense gas flows will fall onto the central galaxy on a free-fall time.
- **Hot accretion** : The alternative is when $t_\mathrm{cool} > t_\mathrm{ff}$, and the cooling of the gas is not efficient enough and the shocked gas will remain within the CGM for a time on the order of t_cool supported via thermal pressure. In the inner regions of the CGM, there will form a region defined using the "cooling radius" that fulfils $t_\mathrm{cool} < t_\mathrm{H}$. This gas will be in a quasi-hydrostatic equilibrium and evolve on the t_cool timescale, giving the gas sufficient time to re-establish hydrostatic equilibrium while cooling and it will accrete smoothly onto the galaxy.

When the CGM transitions to hot accretion, the thermal support and gravitational pull is more or less balanced and the gas will be in a quasi-equilibrium. This transition is called the virialisation of the CGM, as then the CGM will fulfil the virial theorem (Eq. (3.1)).

Following the model proposed by Birnboim & Dekel (2003); Dekel & Birnboim (2006), the virialisation is expected to occur from the inside-out but the CGM is not that idealised in reality. Instead, in a newer approach from Stern et al. (2019, 2020), which is still idealised but instead assuming spherical steady-state cooling flows and including feedback, proposed that showed that the CGM should virialise outside-in. But how the virialisation occurs and the implications for galaxy formation and evolution has not yet reached a consensus and is thus the focus of this work.

1.4 Comparing Simulations

While simulations have been used for many years in science, especially in astrophysics, usually these works have focused on one implementation technique and only varied the physical assumptions. While this may not cause too many issues for many other fields, but if your aim is to simulate the formation and evolution of galaxies, how both the equations are solved and the resolution is determined are usually vital. One of the more famous examples of numerical errors, regarding resolution, is the "overmerging problem" (Klypin et al., 1999). Researchers concluded that dark matter haloes could not survive in dense environments, but in reality it was due to their too low resolution in their N-body simulations. Another classic example is the "Smoothed Particle Hydrodynamics (SPH) instability problem" (Agertz et al., 2007). In this case it was shown that one of the leading numerical implementation techniques SPH, which is still very relevant today, could not properly resolve crucial dynamical instabilities, leading to unphysical pressure forces between steep density gradients. Both of these instances, together with many others, advocate for simulation comparisons that can highlight their differences and possible faults (e.g. O'Shea et al., 2005).

In the beginning of simulations, dark matter could be simulated relatively well with simple simulation setups, as they only required dynamical physics via e.g. gravity (Efstathiou et al., 1985; Davis et al., 1985; Springel et al., 2005). However, with the introduction of gas and stars, more complicated physics had to be included and thus less accurate but much more efficient computational methods were required, such as SPH and AMR (For a more recent review, see Vogelsberger et al., 2020). Over 25 years ago, there was a comparison project done by Frenk et al. (1999) testing a relatively simple astrophysical case where a large cluster in a ΛCDM cosmology was being formed. The consensus of this study was that differences, although seemingly minor, could be identified between codes originating from their different implementations. The implications of this discovery meant that going forward, groups that aim to simulate complicated systems involving e.g. gasdynamics or hydrodynamics have to be extra careful when choosing which method to solve the accompanying equations as this will have an effect on the final results.

Since Frenk et al. (1999), the complexity of simulations has grown, following the complexity of the problems. The importance of comparing different implementations must also be emphasised, as with added complexity there are more equations to solve and thus more discrepancies between methods can occur. There have been many groups that have followed in the footsteps of Frenk et al. (1999) (e.g. Scannapieco et al., 2012; Kim et al., 2014), ensuring that the simulations that are being used are not taken for granted. Instead, the advantages and disadvantages of each method are acknowledged and taken into account when analysing the resulting e.g. galaxies.

Chapter 2

The AGORA Project

AGORA stands for Assembling Galaxies Of Resolved Anatomy, and is an international collaboration spanning over 60 institutions worldwide with more than 160 participants (Roca-Fàbrega et al., 2024). The fundamental goal of the AGORA project is to improve the predictive power of galaxy simulations. This is done by analysing and comparing several high-resolution cosmological hydrodynamic simulations that all assuming the same initial conditions and basic astrophysical processes. By differing in their numerical implementation and some physical model, such as the stellar feedback technique, by comparing both their differences between each other using a common analysis tool called `yt` (see Section 3.1.1) and with observations, the inferred similarities and discrepancies can highlight behaviours uniquely due to the chosen implementation or feedback model. **Note: it must be clarified that none of the simulations used in this work were actually run by the author, instead they were provided by members of the AGORA Collaboration, together with the respective virial radii and centres.**

2.1 CosmoRun

The AGORA CosmoRun suite, is a collection of high-resolution cosmological zoom-in simulations of a galaxy with Milky Way-mass halo 10^{12} $M_\odot$ at redshift $z = 0$ using several different simulation codes. All participating codes had the same initial conditions generated via the adaptive multigrid Poisson solver `MUSIC` (Hahn & Abel, 2011), started from $z = 100$ and were simulated until $z \leq 2$. Note, only some codes were allowed to run further to $z < 2$ as it depended on the availability of both computational and human resources. For a comprehensive overview of their resolution differences, see Figure 1 in Strawn et al. (2024).

2.1.1 Common Physics

The AGORA project has decided that each code in their suite were to keep some common astrophysics components to ensure their differences are not due to these processes Kim et al. (2014). These common astrophysics were:

- **Metallicity-dependent gas cooling**, found via the precomputed cooling table CLOUDY Ferland et al. (2013), provided by the `GRACKLE` chemistry and cooling library Smith et al. (2017), containing the both cooling and heating rates for both the primordial and $1Z_\odot$ metallicity gas as functions of density, temperature and redshift. Then, the $1Z_\odot$ rates are assumed to linearly scale with the gas metallicity and then by adding the primordial contribution, the total cooling and heating rates could be found.

- **Star formation**, all codes assumed that when a parcel of gas exceeded the density threshold of

$n_{\rm H,thres} = 1\ {\rm cm}^{-3}$ then star formation would be possible at a rate of

$$\frac{{\rm d}\rho_*}{{\rm d}t} = \frac{\epsilon_* \rho_{\rm gas}}{t_{\rm ff}} \propto \rho_{\rm gas}^{1.5},$$

where ρ_* and $\rho_{\rm gas}$ are the stellar and gas densities, $\epsilon_* = 0.01$ is the efficiency of the star formation, and finally $t_{\rm ff}$ is the free-fall time of the local gas according to $t_{\rm ff} = \sqrt{3\pi/(32G\rho_{\rm gas})}$. In addition, to avoid artificial fragmentation and unrealistic gravitational collapse, a non-thermal pressure floor was added. While calibrated to match within 1 dex in stellar mass for $z \lesssim 4$, whether the stars formed stochastically or deterministically and the mass of each star particle[1] varied(see Roca-Fàbrega et al., 2021, 2024).

- **Metagalactic ultraviolet background radiation** at $z = 0$, also provided by GRACKLE, comparisons with other models can be found in Section 3.3 of Kim et al. (2014)

- **Stellar IMF**, due to the computational limitations, each star could not be resolved and thus each cell or particle must instead contain a population of stars. To determine the distribution of their masses, as they are born via star formation, a common IMF was used for all codes following Chabrier (2003).

- **Mass return**, the total returned mass per type II supernova event[2] within a star particle[3] was kept the same for all codes at 17.4 $M_\odot$, as was done in Paper II (Kim et al., 2016). Their individual deposit scheme, meaning how the energy and mass is distributed across the ISM, together with their energy and metal yields[4] varied between codes (more details per code in Section 2.1.3 and in Roca-Fàbrega et al. (2021)). Due to the different deposit schemes, metal yields, and stellar feedback models, in order to ensure that the codes still predict comparable metal evolutions, the effective metal yield was used, defined as

$$\text{Effective Metal Yield} \equiv \frac{M_{\rm metal}}{M_*},$$

which is the ratio between the total metal mass and the total stellar mass, i.e. a measure on how efficiently the returned metals enriched the surrounding ISM. The effective metal yield of each code at $z = 4$ can be found in Section 2.1.3.

2.1.2 Calibration

To ensure that each code analysed in the AGORA project all initially generate similar results from the common physical processes and ensure the feedback strength could produce a realistic galactic system, several calibration steps were performed dubbed Cal-1/2/3/4 respectively, see Roca-Fàbrega et al. (2021) for further details and Roca-Fàbrega et al. (2024) for details on AREPO. To start, the radiative cooling/heating, star formation, pressure floor, and SNe feedback were all turned off and each calibration step can be summarised as the following:

- Cal-1 : Tested the gravity and hydro solvers by ensuring convergence of the gas temperature and density distributions. In this run, the system is considered adiabatic as it does not exchange energy with its surroundings but there could still be changes in the entropy due to shocks, meaning variations between codes implies differences in their hydrodynamics solvers, but no significant differences were found.

[1] With a minimum mass of $6.1 \times 10^4\ M_\odot$.

[2] The other sources of stellar feedback in this work, e.g. supernovae type Ia and AGB, are vital in their metal yields but not in mass return (e.g. Scalzo et al., 2014; Khouri, T. et al., 2026) and thus to calculate the total mass return only type II supernovae were considered.

[3] Note that a star particle is not an individual star, due to computational constraints, but instead represents a collection of stars with some total mass, therefore the rates of stellar feedback events (supernovae type Ia, supernovae type II, AGBs etc.) have to be estimated using the stellar IMF.

[4] The metal yields also change depending on the source of stellar feedback (e.g. supernova type).

- Cal-2: Cooling/heating was turned on and tested by comparing the gas temperature and density distributions and confirming convergence between codes. As all the different codes use the same cooling/heating/UVB from GRACKLE and have the same initial metallicity, they should, and for the most part did, agree on the gas distribution in the density-temperature plane. While some artificial features were identified, these would be insignificant when the other physical processes were turned on.

- Cal-3: Cooling/heating remained on but now together with both star formation and pressure floor and all were tested with the total stellar mass but also, as before, with the gas temperature and density distributions. The main purpose of this step was to confirm that the final cosmological simulation results were not dominated by errors from the varying star formation condition. In the end at $z = 7$, all codes converged within 0.5 dex in stellar masses, and showed very similar both stellar mass growth histories and density-temperature PDFs.

- Cal-4: Cooling/heating, star formation, pressure floor, and finally SNe feedback were all turned on and the feedback strength was calibrated for each code by comparing the stellar mass over halo mass ratio versus the value predicted by abundance matching techniques (e.g. Rodríguez-Puebla et al. (2017)). The expected main galaxy stellar mass for a system at $z = 4$ with $M_{200} = 2 \times 10^{11}$ $M_\odot$ is $\sim 1 - 1.5 \times 10^9$ but due this being a relatively eventful epoch for the different galaxies and to allow for more flexibility regarding the stellar feedback scheme, this range was extended to $\sim 1 - 5 \times 10^9$. Ultimately, to reach this calibration goal, each code had to strengthen their stellar feedback but all remaining realistic while also converging to the common M_* range.

2.1.3 Codes Used in This Work and Their Code-Dependent Physics

The AGORA Project is, so far, involved with a total of 13 different codes: ART-I, ART-II, ENZO, RAMSES, CHANGA/-T, GEAR, GADGET-2/3/4, GASOLINE/PKDGRAV, AREPO-T, and finally GIZMO. Unfortunately, not all of the coding groups responsible for these codes have the same access to both computational and human resources, and considering that these simulations are very computationally intensive, their availability for analysis varies. In this work, of these codes, those selected were ART-I, ENZO, CHANGA, CHANGA-T, GADGET-3, GEAR, AREPO, GIZMO, due to their availability. Note, both RAMSES and GADGET-4 were also available but were not included due to lack of time.

2.1.3.1 ART-I

ART-I is an adaptive mesh refinement (AMR) grid code that first appeared in Kravtsov et al. (1997). It has a octree-based, multi-level adaptive mesh, meaning whenever a single cell reaches either a particle or a gas overdensity of 4.0 (four times the gas particle mass $m_{\rm gas} = 5.65 \times 10^4$ $M_\odot$ used in the SPH codes), the cell splits into eight equally sized subcells (Strawn et al., 2024). This refinement is allowed until the minimum resolution of 163 comoving pc. A notable adjustment to ART-I to ensure that it followed the common physics was the stochasticity of the star formation to make certain that it had the same star formation efficiency as the other codes. The feedback scheme used for ART-I was similar to the model presented in Ceverino et al. (2017) and similarly included thermal, kinetic, and radiation pressure feedback Roca-Fàbrega et al. (2021) but also included the later effects of SNe Ia and stellar mass loss following the ISM metal enrichment. The model followed both SNe Ia and SNe II but also AGB stars, but only for metal production, and the effective metal yield was 0.033 at $z = 4$, the injected thermal energy per SN was 2×10^{51} erg, the injected momentum per SN was 2.5×10^6 $M_\odot$km/s, and finally a radiation pressure proportional to 10^{49} erg Myr^{-1} $M_\odot^{-1}$ was added to the total pressure of each cell containing or neighbouring cells with high enough hydrogen column density and stellar particles younger than 5 Myr. In order to fulfil the convergence goal in Cal-4 (see Section 2.1.2), the feedback model from Ceverino et al. (2023) was used but with four times more injected momentum, to compensate for the resolution differences.

2.1.3.2 ENZO

ENZO is a community-driven brick-structured AMR-type code, first made public by Greg Bryan (see e.g. Bryan et al. (2014)). The block-structured AMR scheme originated from the work by Berger & Colella (1989) and works on the principle of refining entire localised rectangular blocks at multiple refinement levels rather than refining cells individually, generally allowing for faster calculations. As with ART, this refinement is also limited to a minimum of 163 comoving pc, to avoid any significant resolution-based differences between the codes. The chosen feedback model used in this version of ENZO followed the one for AMR codes in Kim et al. (2016) where thermal energy, mass, and metals were simply added into the cell, and only this cell, if it contains a 5 Myr old star particle at the time of explosion. This model only considered the stellar feedback from SNe II with an effective metal yield of 0.032 at $z = 4$, thermal energy injection of 5×10^{52} erg/SN. Then, to calibrate this according to the conditions set for Cal-4, the stellar feedback efficiency of ENZO had to be increased from the value shown in Kim et al. (2016), which also better fit the results with those found by Oh et al. (2020).

2.1.3.3 CHANGA / CHANGA-T

CHANGA is a particle-based SPH code, with similar hydrodynamic solving as the code GASOLINE (Menon et al., 2015; Wadsley et al., 2017), with a slight modified implementation. The hydrodynamical properties were solved for the N_{ngb}th (= 64th) neighbours, following the kth nearest neighbour algorithm, via the Wendland C4 kernel (Dehnen & Aly, 2012). In this work, two version of CHANGA are included, both including thermal stellar feedback, but simply CHANGA also including the so-called "superbubble" feedback, see Keller et al. (2014), where the immediate regions around supernovae are superheated. In order to distinguish between these two version, the one using pure thermal feedback is indicated with CHANGA-T. Both versions of CHANGA include thermal energy injection from SNe Ia, with rates from Matteucci & Greggio (1986), and SNe II, with rates from Raiteri et al. (1996), totalling 3.25×10^{51} erg for CHANGA and 8×10^{51} erg for CHANGA-T. Metal yields from SNe and AGB stars were also taken from Raiteri et al. (1996), and the effective metal yields at $z = 4$ were 0.032 and 0.031 for CHANGA and CHANGA-T respectively. The injected thermal energy was distributed among the N_{ngb}th neighbours, and both energy and metals were diffused via the Shen et al. (2010) scheme.

2.1.3.4 GADGET-3

GADGET-3 is the third generation of a series of SPH-type codes all dubbed GADGET, initially introduced in Springel et al. (2001) and in this work the thermal-only version of the modified GADGET3-OSAKA (called simply GADGET-3 in this work) was analysed (Aoyama et al., 2016; Shimizu et al., 2019). Notable modifications for this version includes the density-independent, pressure-entropy formulation of SPH Hopkins (2013); Saitoh & Makino (2013), a limiter on the timesteps (Saitoh & Makino, 2009), a quintic spline kernel (Morris, 1996), and finally the number of neighbouring particles for each SPH particle was limited to 128 ± 8. The stellar feedback was treated by distributing both thermal and kinetic energy across neighbouring gas particles contained inside a hot bubble, the size of which was found from the local gas density, ambient gas pressure, and the feedback energy inside Equations 6-7 in Shimizu et al. (2019). The metals and energy were deposited with a time delay determined by the feedback energy, density, and ambient gas pressure according to the CELIB library (Saitoh, 2017), with the contribution of each source (SN Ia, SN II, and AGB star) being treated individually. The effective metal yield was 0.025 at $z = 4$ and the total injected energy of 4×10^{51} erg/SN was split equally between the thermal and kinetic contribution in order to attain the calibration goal of Cal-4. Additionally, GADGET-3 also included early stellar feedback, meaning thermal energy was injected before the first SNe. Finally, to mimic the effect of metal diffusion, which is not directly implemented, the metals were smoothed over the kernel when metallicity or cooling rate was calculated for each gas particle.

2.1.3.5 GEAR

GEAR is a fully parallel chemo-dynamical tree SPH code which was originally presented in Revaz & Jablonka (2012). GEAR is based on the GADGET-2 code, but with some notable improvements, for example, the pressure-entropy SPH formulation from Hopkins (2013), and individual, adaptive time steps from Durier & Dalla Vecchia (2012) which is an extension of the time limiter by Saitoh & Makino (2009), for the full comparison between GADGET-2 and GEAR see Revaz et al. (2016). The feedback was implemented by depositing both the energy and the yields among the neighbouring gas particles, weighted by the SPH kernel, from SNe Ia and SNe II. The amount of weighted number of neighbours was set to 50, meaning that the stellar ejecta was spread among more or less than 50 gas particles, depending on their spatial distribution. The SNe were assumed to be stochastic and followed a continuous IMF sampling scheme from Revaz et al. (2016) while the feedback scheme itself was blast-wave-like (Stinson et al., 2006) with a delayed cooling time of 5 Myr, injecting 4.5×10^{51} erg/SN. The effective metal yield was forced to be 0.015 at $z = 4$, because the metal production could not be separated from the star formation method and thus it was discovered in later AGORA papers, such as Strawn et al. (2024), that GEAR had consistently a minimum of two times lower metal production than most codes. The yields from the SNe Ia and SNe II were taken from Kobayashi et al. (2000) and Tsujimoto et al. (1995), respectively, and as with GADGET-3, GEAR did not have an explicit metal diffusion process and instead followed the same scheme and smoothed the metals along the SPH kernel when calculating the cooling time and metallicity.

2.1.3.6 AREPO

AREPO is an unstructured moving mesh code that works by combining the principles of SPH and AMR while eliminating some of their weaknesses, such as fluid instability suppression in SPH and the lack of Galilean-invariance in AMR (Springel, 2010). In the Eularian AMR approach the mesh is left stationary but instead in AREPO, the mesh follows the local flow velocity, avoiding the otherwise mesh distortion limitations and allows for full Galilean-invariance. In this work, the AREPO-T version was used, following from the previous AGORA work (e.g. Strawn et al., 2024), meaning that only the thermal feedback from SNe II was considered. It was then implemented by distributing the thermal energy of 2×10^{52} erg/SN, the mass, and the metals, with an effective metal yield of 0.034 at $z = 4$, among 50 ± 1 weighted nearby gas cells via a cubic spline SPH kernel.

2.1.3.7 GIZMO

GIZMO is a mesh-free hydrodynamics code based on the GADGET-3 code but instead using unstructured smoothed volumes discretized by a kernel, called cells, that represent the particles and can change with time (Hopkins, 2015). Similarly to AREPO, this method combines the principles of SPH and AMR by solving the Riemann problem across the effective shared faces between all neighbouring particles. The mesh-free method allows for superior angular momentum conservation over other methods (such as moving mesh), no required artificial diffusion terms, and automatic resolution adaptation but suffers from added grid noise. The stellar feedback for GIZMO only considered SNe II and was based on the model from Hopkins et al. (2018) which assumed mechanical feedback, meaning both kinetic and thermal energy were considered and the distribution of energy and momentum occurred among gas cells within each star particle kernel and was conserved by considering the evolutionary stage of the SN blast wave. The rate of SNe was determined by two functions, first a decaying power-law fit (from Lupi et al., 2020) for star particles older than 5.089 Myr then for younger stars a constant rate set by the maximum value in the power-law. Finally, to ensure that GIZMO fulfilled the Cal-4 requirements, the total amount of injected energy per SN was chosen to be 5×10^{51} erg/SN, with the thermal and momentum contribution being dependent on their respective fractions of the total energy f_T and f_K, determined by several factors described in Hopkins et al. (2018). The effective metal yield was chosen to be 0.033 at $z = 4$.

2.1.4 The Last Major Mergers and Timing Discrepancies

It was found in Paper IV (Roca-Fàbrega et al., 2024) that the merging histories and the time of merging between the codes were slightly different, even in the dark matter only (DMO) runs. They concluded that the two most likely causes for this discrepancy were a small variation in angular momentum distribution at high redshift and that the numerical integration of the equations of motion had a small timing mismatch. The latter was found by noticing that the GEAR-DMO run had a major merger at around $z \sim 4.2$ while most other codes were seen to merge at the expected $z \sim 4.5$. Due to the lack of baryonic physics in this run, this must have been due to how the equations of motions were treated, although note that it was found to not be a fault of the code itself but rather user input. An upcoming AGORA paper, labelled Paper IX.1 and Paper IX.2, has analysed this major merger further and is currently in preparation.

The effect of these timing discrepancies will be noticeable in the final results as the codes can not be as easily compared at the same redshift, due to them possibly existing in slightly different stages of recovery from the major merger event. To avoid this issue, the redshift that will be most relevant for comparison, especially in projection plots, were chosen to be $z = 3$ and $z = 1$, following from e.g. Paper VI (Strawn et al., 2024), significantly long after or before a major merger to avoid possible differences stemming from this timing discrepancy.

Chapter 3

Methodology

3.1 Tools

3.1.1 yt

Due to the immense size and complexity of the data that the different AGORA simulations produce, it was decided, as described in the AGORA flagship paper (Kim et al., 2014), that a common analysis tool called `yt`(Turk et al., 2011; Turk & Smith, 2011; Turk, 2013) was to be used. This allowed for much easier navigation of the data, focusing on the physical descriptions rather than the computational. This open-source astrophysical analysis toolkit is driven by, and for, the galaxy simulation community. Since its release, it has been supported and greatly improved with an emphasis on easing the physical questions by offering methods for e.g. visualisation, region selection and analysis, and data handling with units. In this work, `yt` was mostly used for loading the simulation data, ensuring unit consistency, and creating new easily accessible derived physical quantities, such as gas pressure, hydrogen density etc. In addition, `yt` was also used to produce thin projections of density-weighted line of sight averages.

3.2 Defining the CGM

The boundaries of the CGM, as with many structures of astronomy, are not well defined and blend together with both the ISM and the IGM. These regions are in turn not well described either, but can be approximated using the virial radius $R_{\rm vir}$ (Bryan & Norman, 1998), defined as the radius within which the galaxy fulfils the virial theorem

$$2K + U = 0, \tag{3.1}$$

where K and U are the total kinetic and potential energy respectively. Within $R_{\rm vir}$, the galaxy can be considered detached from the Hubble expansion and gravitationally bound (Mo et al., 2010).

While most work on the CGM agree on the outer boundary as $R_{\rm vir}$, the choice of the inner radius is much more unclear but is usually somewhere between $0.1R_{\rm vir}$ and $0.2R_{\rm vir}$ (see e.g. Faerman et al., 2022; Shen et al., 2013). In this work, the inner CGM radius was defined as 0.2 $R_{\rm vir}$, to safely avoid contamination from the central galaxy. Worth noting is that in AGORA papers where the CGM was included, it was instead usually defined as 0.15 $R_{\rm vir}$ (e.g. Paper VI Strawn et al., 2024). The choice of this new definition is motivated by the recent discovery of greatly varying stellar disk sizes (Jung et al., 2025) between codes. Although the extend of the gaseous disk has not yet been investigated, it is believed to extend past the stellar component (van der Kruit & Freeman, 2011). In this work minimising ISM contamination is especially important due to it containing gas with very different properties (especially $t_{\rm cool}/t_{\rm ff}$), and thus a safer option was chosen. For the evolution of the virial radius in each code, please see Figure 3.1, and note that both virial radii and galaxy centres were provided to the author by members of the AGORA Collaboration.

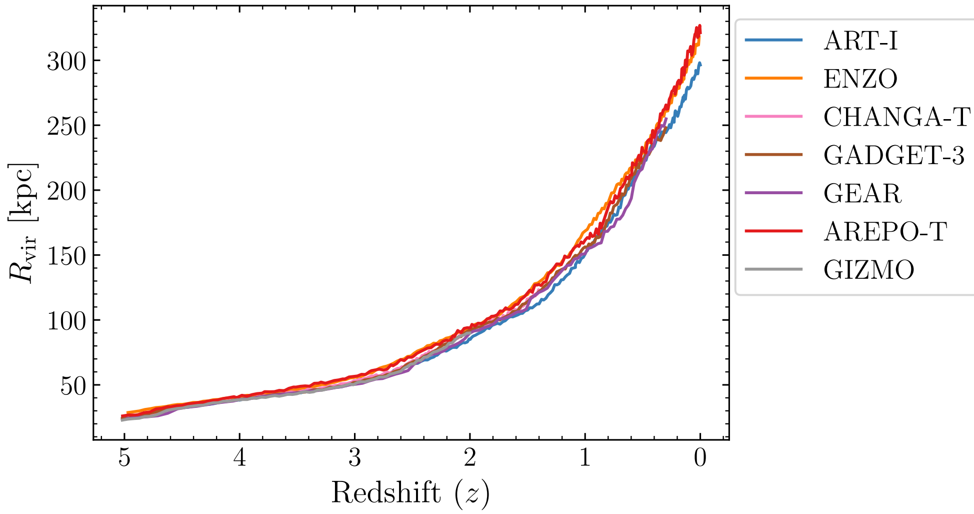

Figure 3.1: The virial radius against redshift for each code. Note that the virial radii were not derived by the author of this work but rather members of the AGORA Collaboration following Bryan & Norman (1998). In addition, they were found using the dark matter version of each code, meaning the critical density was only considering dark matter and not baryonic matter.

3.2.1 CGM Gas Phases

In this work, the temperature ranges for the CGM thermal gas phases were simplified into just three groups, defined as:

- Cold Gas : $T < 2 \times 10^4$ K : Chosen to include the "cooling track" gas of $\sim 10^4$ K that tracks the minimum gas temperature when cooling dominates over heating, due to photoionization (see Figure 5 in Paper III Roca-Fàbrega et al., 2021).
- Warm Gas : 2×10^4 K $< T < 3 \times 10^5$ K : An intermediate temperature range, meant to include all gas that is neither cold nor hot, as per the observational evidence implying that this phase is a transition between the two more extreme phases (Tumlinson et al., 2017).
- Hot Gas : $T > 3 \times 10^5$ K : Includes all virialized gas, but due to the virial temperature being dependent on halo mass, it must be slightly lower than the expected $T_{\rm vir}(z = 0) \sim 6 \times 10^5$ K (McClain et al., 2024), as the galaxies were also analysed long before they reached their final dark matter haloes.

3.3 Modelling the Cooling Flows

The analytical model used in this work is the same one as Stern et al. (2020), and models the two important timescales, $t_{\rm cool}$ and $t_{\rm ff}$, that dictate the transition between cold to hot accretion in the CGM.

3.3.1 Cooling and Free-Fall Times

As explained in Section 1.3.3, the ratio between the cooling time and the free-fall time of the gas within the CGM is a very important probe into the evolution of the galaxy. In this work, the cooling time is defined as

$$t_{\rm cool} = \frac{P}{(\gamma - 1) n_H^2 \Lambda}, \tag{3.2}$$

where γ is the adiabatic index assumed here to be 5/3 from the monatomic gas, P is the gas pressure, n_H is the hydrogen density, and finally Λ is the cooling function (Eq. (3.3)). The gas pressure was found from the ideal gas law and thus $P = \rho k_B T/\mu m_H$ where ρ and T is the gas density and temperature respectively, μ is the mean molecular weight (from `GRACKLE`), and m_H is the hydrogen mass. Then, the hydrogen density was found with $n_H = X\rho/m_H$ where X is the hydrogen fraction, here assumed to be the primordial value $X = 0.76$ as it is the standard in `GRACKLE`. Finally, the cooling function was defined as the difference between the total cooling and heating rate

$$\Lambda = C - H = C_{\text{prim}}(\rho, z, T) - H_{\text{prim}}(\rho, z, T) + Z[C_{\text{metal}}(\rho, z, T) - H_{\text{metal}}(\rho, z, T)], \tag{3.3}$$

where Z is the metallicity relative to the solar metallicity, and prim and metal indicate the interpolated primordial and metal cooling/heating rates from `GRACKLE`, all as functions of density, redshift, and temperature. The free-fall time was defined as

$$t_{\text{ff}} = \frac{\sqrt{2}r}{v_c}, \tag{3.4}$$

where r is the radius from the centre, and v_c is the circular velocity defined as $v_c = \sqrt{\frac{GM_{\text{g}}(<r)}{r}}$ with G being the gravitational constant, and $M_{\text{g}}(< r)$ is the enclosed gravitating mass giving rise to the velocity, which in this case will mostly consist of dark matter due to its dominant contribution to matter (Planck Collaboration et al., 2020). By then taking the ratio between (Eq. (3.2)) and (Eq. (3.4)), the virialisation quantity $t_{\text{cool}}/t_{\text{ff}}$ is defined.

3.3.2 Accounting for Different Phases

An important consideration that was encountered in this work is that $t_{\text{cool}}/t_{\text{ff}}$ was especially sensitive to the phase of the gas, if it tracks the cool, dense gas or the hot, diffuse gas. This is obvious when considering the parameters that go into the cooling and free-fall times, e.g. the strong density dependence of the cooling times. This meant that if simply the arithmetic median or mean were to be taken at each time step, it would include a mix between these two gas phases. The moment when $t_{\text{cool}}/t_{\text{ff}} = 1$ would thus be dominated by the hot and diffuse gas, and be predicted much earlier and not representing the true state of the gas. To circumvent this, the weighted median was instead used, defined as the element x_k in an ordered set of n values with n positive weights w_i, where $\sum_{i=1}^{n} w_i = 1$, which fulfils both

$$\sum_{i=1}^{k-1} w_i \leq 1/2 \text{ and } \sum_{i=k+1}^{n} w_i \leq 1/2.$$

Then, by weighting for mass, the cold and dense gas was emphasised, or by weighting for volume, the hot and diffuse gas could be focused. In this work the main focus was the mass-weighted median, as this ensured that the majority of the baryonic mass was fairly represented, but the volume equivalent is also included in the paper appendix.

Chapter 4

Paper

MNRAS 000, 1–13 (2026) Preprint 16 June 2026 Compiled using MNRAS LaTeX style file v3.2

The *AGORA* High-resolution Galaxy Simulations Comparison Project. XIV. Formation of the Circumgalactic Medium

Isak Lindh,[1★] Oscar Agertz,[1] Santi Roca-Fàbrega,[1] Víctor Rufo-Pastor,[1] et. al.
[1]Lund Observatory, Division of Astrophysics, Department of Physics, Lund University, SE-221 00 Lund, Sweden

Accepted XXX. Received YYY; in original form ZZZ

ABSTRACT
The circumgalactic medium (CGM), the extended gaseous halo surrounding galaxies, plays a central role in the cycling of baryons between galaxies and the intergalactic medium. Observations are not yet able to reveal a complete census of the CGM around Milky Way (MW)–mass galaxies, making theoretical predictions crucial. In this work, we investigate the formation and evolution of the CGM using eight cosmological zoom-in simulations of MW–mass galaxies. The simulations share identical initial conditions, cosmology, star formation thresholds, and heating/cooling prescriptions, but differ in numerical methods and stellar feedback implementations, leading to variations in the baryon cycle and CGM properties. At the current epoch, the models predict CGM mass fractions in the range of ∼ 20–50 per cent of the cosmic baryon fraction. We find that the relative contributions of hot ($T \sim 10^6$ K), warm ($T \sim 10^5$ K), and cold ($T \lesssim 10^4$ K) phases vary strongly across simulations. Some models develop a hot CGM due to starbursts induced by major mergers already at $z \gtrsim 4$, earlier than expected from accretion shocks, whereas others predict a later transition ($z \lesssim 1.5$). Interestingly, these latter models, despite apparently weaker feedback, often regulate the total baryon fraction more efficiently, with the cosmological value reached only at several virial radii. This highlights the differences between preventive versus ejective feedback models. These discrepancies do not manifest themselves as obviously for the epoch when the CGM virialises, with gas cooling times superseding dynamical times. Instead, most codes show a similar halo wide virialization ranging from $z \sim 2$ to $z \sim 3$, although with some margin of spread likely due to feedback differences. This is in contrast to the inside-out and outside-in scenarios predicted by previous work.

Key words: methods: analytical – methods: numerical – galaxies: evolution – galaxies: formation - galaxies: haloes

1 INTRODUCTION

The existence of gas around galaxies, henceforth the circumgalactic medium (CGM), was proposed many decades ago, first in Spitzer (1956), see also Münch & Zirin (1961). Since then, how it forms and evolves via gas accretion, feedback driven outflows, magnetic fields, and cosmic rays etc., are not yet fully understood (Faucher-Giguère & Oh 2023). As the mediator between the interstellar medium (ISM) and the intergalactic medium (IGM), the CGM is the stage for the galactic baryon cycle and is therefore essential for the formation and evolution of galaxies (Tumlinson et al. 2011; Woo et al. 2013; Woods et al. 2014).

Observations of the CGM have revealed a complicated structure made from multiphase gas, the coexistence of gas with different temperatures, densities, and ionization states (Putman et al. 2012; Peroux & Nelson 2024). Identifying and characterizing these different phases is an ongoing endeavour, with one focus being constraining their individual CGM mass contribution over a range of galaxy masses, as they have been found to depend on the size of the galaxy (for a recent review, see Chen & Zahedy 2026). Due to the diffuse and ionized nature of the CGM, constraining its contents via emission-based observations has been challenging (Cantalupo et al. 2019). Emission strength has a density dependence of n^2 (van de Voort & Schaye 2013), meaning collected emission lines will primarily be from dense regions, and the signal from the diffuse hot gas will be difficult to discern. In addition, emission strength also has a strong inverse redshift proportionality of $(1 + z)^{-4}$. Therefore, in an emission-based observation of two similar galaxies, one at $z = 0$ and the other at $z = 2$, the latter would have 81 times lower emission strength. Observational efforts based on emission , particularly in X-ray and gamma-ray bands, have largely been limited to the Milky Way and a small number of nearby galaxies, restricting such studies to low-redshift systems (Gupta et al. 2012; Zhang et al. 2021).

In contrast, absorption-line spectroscopy along the line of sight to bright background sources, most commonly quasars, has emerged as a primary method for probing the CGM, see e.g. the COS-Halos Survey (Tumlinson et al. 2013; Werk et al. 2016) or the more recent Project AMIGA (Lehner et al. 2020a,b). This method allows for a wider selection of densities, sensitivity to exceedingly diffuse columns of gas $N \simeq 10^{12}$ cm^{-2}, and no dependence of detection limits on redshift nor galaxy luminosity (Tumlinson et al. 2017). However, it relies on the chance alignment of a foreground galaxy with a suitable background source, making such configurations relatively rare. Moreover, each galaxy–quasar pair typically provides only a single line of sight, limiting spatial sampling and contributing significant uncertainty to inferred CGM properties.

★ E-mail: isak.lindh@hotmail.com

Despite the uncertainties, these absorption-line surveys have found that a large amount of the expected baryonic mass, relative to the cosmic baryon fraction, is unaccounted for within the bound halo of nearly all galaxies, referred to as the "missing baryon problem" (e.g. McGaugh et al. 2010). One likely answer is that the gas resides further out in a hot corona that is difficult to observe (Nicastro et al. 2023). The problem is less significant, or even non-existent, in more massive galaxies $M_{\rm vir} \sim 10^{12.5} - 10^{13} M_{\odot}$, galaxy groups $M_{\rm vir} \sim 10^{13} - 10^{14} M_{\odot}$, and galaxy clusters $M_{\rm vir} \gtrsim 10^{14} M_{\odot}$, where observations can account for the cosmic baryon fraction (McGaugh et al. 2026). Due to their size and brightness, individual hot coronae can be observed, allowing easier detection of their baryonic content (Zhang, X. et al. 2026) . For smaller galaxies, with Milky Way-mass and less, some recent observational attempts have been successful (e.g. Das et al. 2019, 2020), although both the amount of missing baryons and the observational uncertainty rapidly grow with lower mass. A census for where these missing baryons are in these galaxies is less clear, but seems to be directly tied to the physical processes behind the baryon cycle (Bregman et al. 2022), hence a focus of this work.

The source of this hot gaseous halo can be explained in theory with a simple model that assumes spherical accretion of gas (Birnboim & Dekel 2003). In this scenario, if the dark matter halo is massive enough ($> 10^{11}$ M$_{\odot}$), the accreting gas will be accelerated to supersonic velocities. As this supersonic gas encounters the CGM, accretion shocks develop and propagate outwards, converting part of their kinetic energy into thermal energy for the infalling gas with a temperature on the order of the virial temperature[1]. The stability of these accretion shocks depends on the balance between the thermal pressure support behind the shock front, and therefore the efficiency of gas cooling, and the gravitational pull of the infalling gas (Mo et al. 2010).

The Birnboim & Dekel (2003) model for gas accretion is based on idealized, spherical gas accretion and therefore ignores the many large- and small-scale physical processes known to complicate this picture (Faucher-Giguère & Oh 2023). To test the significance of these different baryonic physics, e.g. magnetic fields (e.g. Rintoul et al. 2025), or cosmic rays (for a recent review, see Ruszkowski & Pfrommer 2023), on the formation and evolution of galaxies, numerical simulations are key (e.g. Feldmann & Bieri 2025).

Stellar feedback is a vital component of the baryon cycle in galaxies of Milky Way-mass or lower (Fielding et al. 2017). These outflows suppress star formation, helping to solve the overcooling problem (White & Frenk 1991), either by removing star forming gas or by preventing gas accretion from the CGM (e.g. Somerville & Davé 2015). The implementation of stellar feedback and how the energy and matter should be injected back into the system is not well understood (see e.g. Rey et al. 2025). But the effects of using different stellar feedback models are expected to appear in the CGM due to its strong involvement in the baryon cycle for Milky Way-mass and smaller galaxies (Wright et al. 2024). The efficiency of the stellar feedback outflows will affect the fractions of metals, baryons, and energy that are being pushed out into the CGM or lost beyond into the IGM. More metals provide more efficient cooling, decreasing stability, while hot gas and energy provides pressure support, and momentum provides turbulence, all of which generally hinders CGM flows (Faucher-Giguère & Oh 2023). Testing and comparing predictions from different simulation codes and feedback models is therefore crucial in order to constrain our understanding of stellar feedback in galaxy formation.

This work is a continuation on a previous paper within the AGORA (Assembling Galaxies of Resolved Anatomy) Collaboration by (Strawn et al. 2024, hereafter referred as Paper VI). This work centred on the evolution of the baryon cycle and virialisation, in order to see if they can be used to distinguish between galaxies using different stellar feedback and numerical implementation. Past AGORA papers have set much of the ground work for this endeavour, and the following were most relevant for this work: Roca-Fàbrega et al. (2021), henceforth Paper III; Roca-Fàbrega et al. (2024), henceforth Paper IV; Rodríguez-Cardoso et al. (2025), henceforth Paper VII; Jung et al. (2025), henceforth Paper VIII; Nguyễn et al. (in prep.), henceforth Paper IX.1 or Paper IX.2 (contains two parts) . For a complete collection of all the AGORA work so far, please see the website The AGORA Project.

This paper is structured as follows. Section 2 includes a brief introduction of the simulation codes; how the CGM was defined; and the definitions for the accretion timescales, $t_{\rm cool}$ and $t_{\rm ff}$.;In Section 3, the evolution of the CGM was compared between simulations via the key CGM properties, such as density, temperature, and metallicity, together with the baryon distribution and virialisation. In Section 4, we examine the results together with differences and similarities between codes in greater detail and in a broader context. Specifically, we discuss how the choice of numerical implementation and stellar feedback model shapes the formation, evolution and stabilisation of the CGM. Finally, in Section 5, the core results and points of this work are presented, together with final comments on future AGORA work and the importance of code comparisons.

2 METHOD

2.1 The AGORA CosmoRun Simulation Suite

The AGORA Collaboration has assembled a suite of high-resolution cosmological hydrodynamical zoom-in simulations of Milky Way-mass galaxies called the AGORA CosmoRun simulations (see Paper III and Paper IV). Each simulation used a different numerical implementation and stellar feedback prescription (see Table 1, or Paper IV), but with identical initial conditions, star formation requirements[2], and heating/cooling prescription (Smith et al. 2017). To ensure reasonable consistency for the stellar properties for $z \geq 4$, each simulation was calibrated in several steps, see Paper III. Out of the many participating codes, eight were selected for this work[3], characterised primarily by their hydrodynamic solvers: Adaptive Mesh Refinement (AMR) (ART-I and ENZO); Smoothed Particle Hydrodynamics (SPH) (CHANGA, CHANGA-T[4], GADGET-3, and GEAR); Moving Mesh (MM) (AREPO-T[5]); and Mesh-Free (MF) (GIZMO). For further details regarding each individual code, see Paper III and Paper IV.

[1] $T_{\rm vir} = (\mu m_{\rm p}/2k_{\rm b}) \times (GM_{\rm vir}/R_{\rm vir})$, which for a Milky Way-mass galaxy at $z = 0$ with $M_{\rm vir} \approx 10^{12} M_{\odot}$ and $R_{\rm vir} \approx 260$ kpc amounts to $T_{\rm vir} \approx 6 \times 10^5$ K

[2] Note that they had identical conditions for star formation, e.g. threshold density, formation efficiency etc., but varied in their either stochastic or deterministic nature, see Paper III and Paper IV

[3] Note that the two current codes that were not included were RAMSES and GADGET-4, both due to lack of time.

[4] Note that two versions of CHANGA were used, where CHANGA-T included only thermal feedback, hence the "-T" for clarity.

[5] Same as with CHANGA-T.

Table 1. Each code included in this work, together with their numerical implementation and their stellar feedback type(s) with the respective feedback parameters, and final snapshot redshift. Note that T = Thermal feedback, K = Kinetic feedback, RP = Radiation Pressure feedback, S = Superbubble, DC = Delayed Cooling feedback, for further details on the feedback mechanisms, and the parameter definitions ($P_{\rm rad}$, $t_{\rm hot}$, f_T, f_K) and how they were implemented, see Paper III and VI. In addition, it must be clarified that the final snapshot redshift are not an indication on the codes' respective performance but rather the availability of both manpower and CPU time for the responsible coding group.

Code Name (Numerical Implementation)	Feedback Type: Feedback Parameter	Final Snapshot Redshift
ART-I (AMR)	**T**: 2×10^{51} erg; **K**: 2.5×10^{6} $M_\odot$ km s^{-1}; **RP**: $P_{\rm rad}$	0.0
ENZO (AMR)	**T**: 5×10^{52} erg	0.0
CHANGA (SPH)	**T**: 3.25×10^{51} erg; **S**: Details in Keller et al. (2014)	1.0
CHANGA-T (SPH)	**T**: 8×10^{51} erg	1.4
GADGET-3 (SPH)	**T**: 2×10^{51} erg; **K**: 2×10^{51} erg; **RP**: $2.5\times10^{48}M_\odot^{-1}$; **DC**: $t_{\rm hot}$	0.3
GEAR (SPH)	**T**: 4.5×10^{51} erg; **DC**: 5 Myr	0.3
AREPO-T (MM)	**T**: 2×10^{52} erg	0.3
GIZMO (MF)	**T**: $f_T\cdot5\times10^{51}$ erg; **K**: $f_K\cdot5\times10^{51}$ erg	2.0

2.2 Defining the CGM

In order to analyse the CGM, one must first define its boundaries, which is not trivial due to its poor constraints and blurry interface with the ISM. Generally, the outer boundary is set as $R_{\rm vir}$ or R_{200c}, following from Bryan & Norman (1998) same as previous AGORA work, but the inner boundary is more disputed, with the most common being $0.1R_{\rm vir}$ (e.g. Hafen et al. 2019), $0.15R_{\rm vir}$ (e.g. Paper VI), or $0.2R_{\rm vir}$ (e.g. Shen et al. 2013; Mitchell et al. 2017). In this paper, the chosen inner and outer boundaries were $0.2R_{\rm vir}$ and $R_{\rm vir}$ respectively. This choice was made primarily because beyond $0.2R_{\rm vir}$ the CGM seems to become sufficiently distinct from the ISM (Kacprzak et al. 2025). In addition, each galaxy from the different simulation codes had slightly different sizes of their central concentrations, see Paper VIII, and nearly identical virial radius evolution (see Figure 4 in Paper IV). This boundary definition therefore ensured minimal ISM contamination while keeping equitable treatment. A fault that is caused by this definition is the so called pseudo-evolution (e.g. Liang et al. 2016; Hafen et al. 2019, Rufo-Pastor et al. in prep.). For the baryonic cycle analysis, this mistake is made the same for all codes, meaning comparisons will still be fair. Further consideration is beyond the scope of this work but is worth considering and investigating in the future.

2.3 Steady-state Virialisation

In order to quantify the virialisation of the CGM, the metric $t_{\rm cool}/t_{\rm ff}$ was used, following from influential work by Rees & Ostriker (1977); Silk (1977); White & Rees (1978), and later Birnboim & Dekel (2003); Dekel & Birnboim (2006). Note that these equations all assume a steady state system with spherically symmetric ideal fluid, lacking any terms that consider angular momentum, magnetic fields (not applicable here), viscosity, or thermal conduction. The cooling time, $t_{\rm cool}$, is defined as

$$t_{\rm cool} = \frac{P}{(\gamma-1)n_H^2\Lambda}, \quad (1)$$

where γ is the adiabatic index (chosen here to be 5/3, assuming primarily monatomic gas), $n_H = X\rho/m_{\rm p}$ is the hydrogen density (with X being the hydrogen mass fraction, ρ the gas density, and $m_{\rm p}$ the proton mass), $\Lambda = C - H$ is the cooling function defined as the difference between the cooling rate C and heating rate H, and finally P is the pressure given by the ideal gas law as $P = \rho k_B T/\mu m_p$, where k_B is Boltzmann's constant, T is the temperature, and μ is the mean molecular weight. In the AGORA suite of simulations, they all treated cooling, heating, and mean molecular weight the same way using the cooling library GRACKLE (Smith et al. 2017) that uses a precomputed CLOUDY table (Ferland et al. 2013; Ferland et al. 2023) which interpolates C, H, and μ using the gas density, metallicity, and the redshift.

The free-fall time, $t_{\rm ff}$, is defined as

$$t_{\rm ff} = \frac{\sqrt{2}r}{v_c}, \quad (2)$$

where r is the radial distance from the galactic centre, and v_c is the circular velocity defined by $v_{\rm c} = \sqrt{GM(<r)/r}$ where G is the gravitational constant and $M(<r)$ is the enclosing mass within the radial distance r.

3 RESULTS

3.1 Comparing Snapshot Projections

In order to get a qualitative overview for each code, projection plots are shown in Figure 1. These projections focus on the denser regions in the CGM by taking their density-weighted average and removing the central galaxy ($< 0.2R_{\rm vir}$)[6]. This is done for $z = 5$, 3, 1, and 0.3, chosen in order to avoid the major merger timing discrepancy at $z\sim4$ and $z\sim2$, see Paper IV.

From the projections, it can be seen that each code has noticeable cold ($T \lesssim 2\cdot10^4$ K) and dense ($n > 3\times10^{-3}$ cm^{-3}) flows that accrete along the z-axis in the earlier times, at $z = 5$ and 3. At $z = 1$ there were still some denser regions present, most likely satellite galaxies, for a further analysis see Paper VII. By $z = 0.3$, the simulations that reach this redshift (see Table 1), have lost nearly all significant dense concentrations, although it can be seen that ART-I and ENZO still have some denser regions within the CGM, while GEAR can be seen to have a few dense clumps left with seemingly trails of denser gas following them, possibly again interacting satellites, but only one is well within the CGM. From Paper VII, it was found that the satellites in GEAR retained much more of their gas from inefficient stripping which could explain their higher density. While the AMR codes and

[6] Note that these are not full projections and instead the thickness along the line of sight axis has been shortened to just $R_{\rm vir}$, instead of the using the width of $3R_{\rm vir}$, making these instead thin projection. This is done mostly to minimize the gas that might exist either in the foreground or the background along y that could otherwise contaminate the CGM, although this had a relatively small effect.

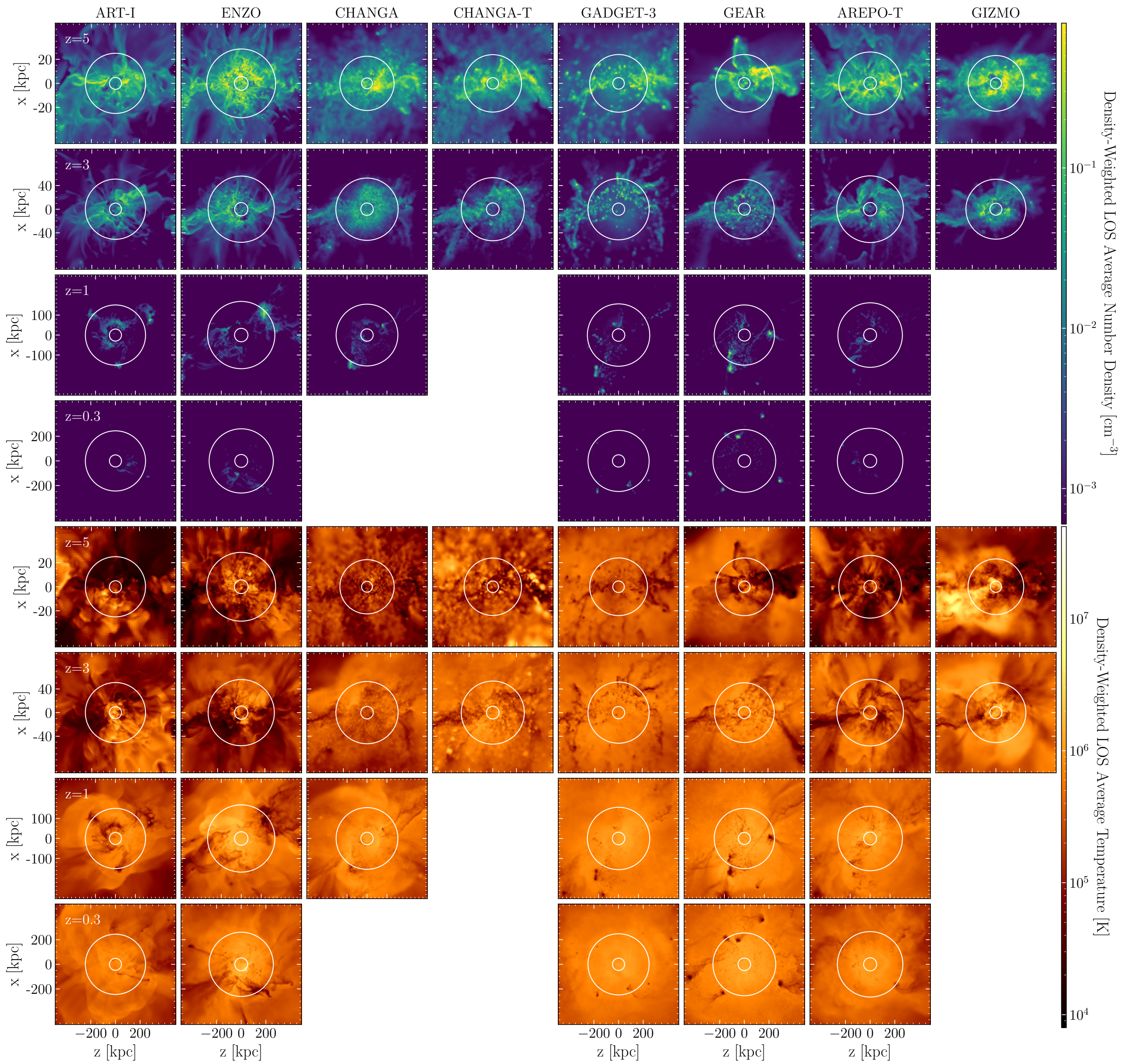

Figure 1. Density-weighted line of sight average number density (above) and temperature (below), along the y-direction, at $z = 5$, 3, 1, and 0.3 from the eight CosmoRun codes included in this paper, centred on their respective galactic centre defined in earlier AGORA papers but with the galaxy removed (i.e. $R < 0.2R_{\rm vir}$). The CGM boundaries are indicated with white circles.

AREPO-T keep fairly filamentary flows of dense gas, it can be seen in the SPH codes that their inflows instead form denser clumps. It has been previously studied, in e.g. Paper III, that the SPH codes, especially GADGET-3 and GEAR, generally form more clumpier regions than the AMR codes.

From the temperature projections, many of the same structures as in the density are repeated, because the denser regions generally cool faster and thus are colder. It can be seen, clearly in $z = 3$, that the AMR and SPH codes differ significantly in their temperature within the CGM, with the AMR codes having more prominent cold regions while the SPH codes are much more heated. For the other codes, AREPO-T seems to be more similar to the AMR codes with colder and denser clumps, while GIZMO is more like the SPH codes with hotter regions. Although how they solve the Euler equations is similar in spirit where both behave like a blend of SPH and AMR, their implementation differences favour one more than the other. The higher CGM temperatures in the SPH codes and GIZMO result in a more diffuse medium, increasing thermal support and making cooling less efficient,

3.2 The CGM Mass Distribution

In order to see the properties of the gas mass and volume in the CGM, the mass fractions of 5 different gas properties were presented in 2D histograms together with the respective mass- and volume-weighted medians, see Figure 2. Starting with the top panels, tracking

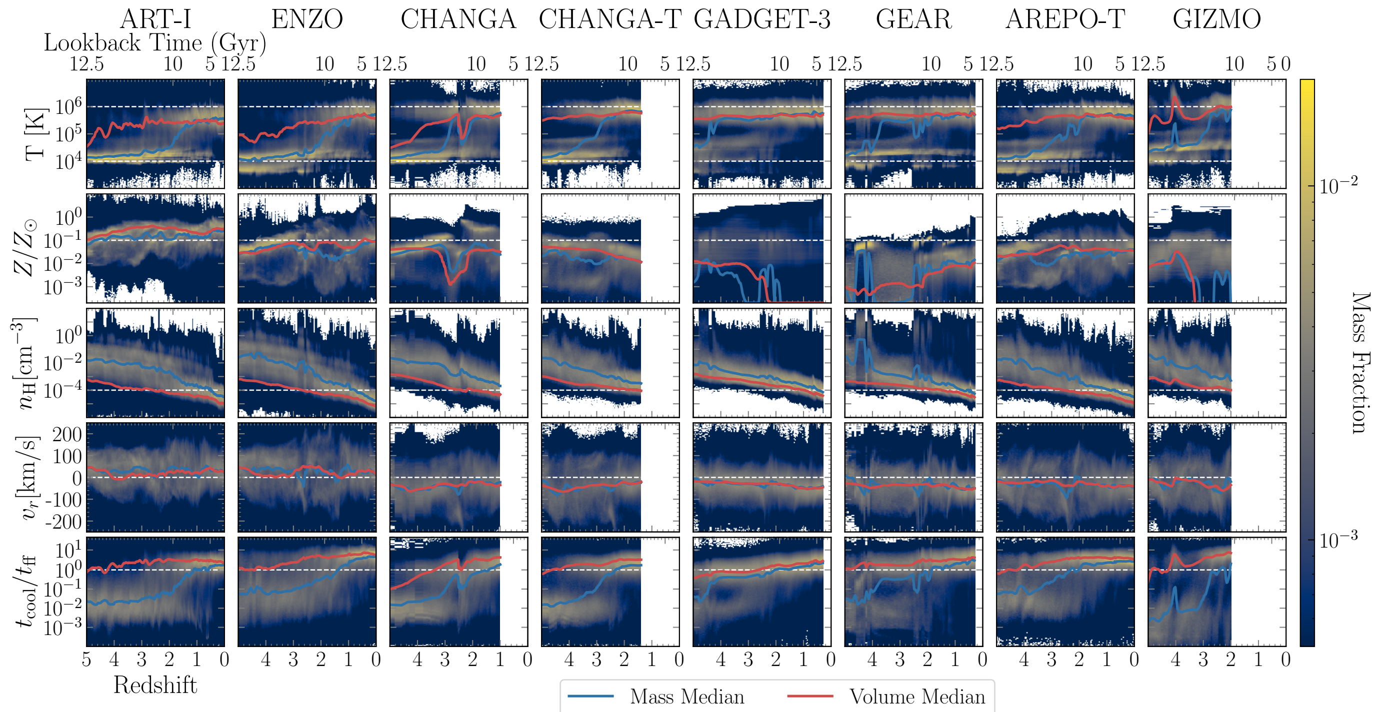

Figure 2. 2D histograms showing the mass fraction distribution over redshift (and lookback time) for the CGM properties: temperature T; relative metallicity $Z/Z_\odot$; hydrogen density $n_{\rm H}$; radial velocity v_r; and finally the virialisation metric $t_{\rm cool}/t_{\rm ff}$. Also included are the mass- and volume-weighted medians (blue and red respectively) of the mass distributions evaluated at each available z. Note that some codes do not reach $z = 0$ and instead end their simulation run earlier, this is independent on their performance but rather availability of resources.

temperature, all codes exhibit the expected behaviour where most mass initially belonged to the primary cooling curve, or "cooling track" around $T \sim 10^4$ K, the minimum gas temperature where cooling dominates over heating (see Figure 5 in Paper III). All codes subsequently transition to the expected virial temperature for Milky Way-mass galaxies of $T_{\rm vir} \approx 6 \times 10^5$ K at $M_{\rm vir} \sim 10^{12}$ $M_\odot$ (McClain et al. 2024). The transition occurs for the mass-weighted median (tracking dense gas) for the AMR codes at around $z \sim 2$ and for most of the SPH codes, AREPO-T, and GIZMO earlier at $z \sim 3$, but for GADGET-3 and GEAR it happened even sooner, closer to $z \sim 4$. Due to the different feedback models used in ART-I and ENZO, and the similar models between ART-I and GIZMO, these differences are most likely rooted in their numerical implementation rather than stellar feedback model. Furthermore, ART-I and ENZO showed a more continuous transition between the cooling track and the virialisation track, due to their ability to include very low density gas via their grid-based implementation (see Paper III). The particle-based codes did not share this feature and instead had much simpler, segmented structures.

The second row of panels shows the relative metallicities $Z/Z_\odot$, with clear discrepancies between codes. Note that due to the difference in final snapshot redshift of each code (see Table 1), codes that end earlier can only be compared with the other codes up until their last redshift, given the other code also reach it. Based on their metallicity trends, the codes can be divided up into three groups. First, ART-I, ENZO, and AREPO-T have an overall increasing metallicity evolution with varying dispersion and magnitudes. This implies that these codes were more efficient at enriching their CGM via outflows, consistent with results from Paper VI. CHANGA has initially an increasing metallicity but after the delayed merger-induced starburst at $z \sim 3$ (see Appendix C in Paper IX.1), gas was rapidly accreted into the central galaxy, initially depleting the CGM of metallicity, although note the significant high metallicity gas later ejected. CHANGA-T has a decreasing trend of metallicity, implying that the pristine inflows had a slight advantage over the metal-rich outflows. Finally, GADGET-3, GEAR, and seemingly GIZMO[7] that show a sudden significant metallicity loss.Based on these divisions, their similarities in trends seem to not have an obvious connection to their respective feedback model. For example, the similarity between ENZO and AREPO-T is not surprising, as they both used pure thermal feedback, but with the inclusion of strong kinetic feedback in ART-I and a similar trend implies that feedback-based differences can not be deduced via their mass distributed metallicity trends. Separating the codes depending on their magnitude, the groupings change slightly: ART-I is alone with the most, where the majority of the mass stayed above $10^{-1} Z_\odot$ for the majority of the time; ENZO, CHANGA, CHANGA-T, and AREPO-T also had a relatively high metallicity but stayed well within $10^{-2} Z_\odot$ and $10^{-1} Z_\odot$; and finally GADGET-3, GEAR, and GIZMO with metallicities $< 10^{-2} Z_\odot$ for most of the time. The low metallicity in GEAR was anticipated from both its implementation, decreasing it by a factor of 2 (see Paper III), and from its reported slow and inefficient outflows of metals in Paper VI. As with the trend, possible connection between codes remain unclear, but the high metallicity from ART-I, ENZO, and AREPO-T are consistent with Paper VI. The differences in both metallicity trend and magnitude between CHANGA and CHANGA-T can be

[7] Due to the limited snapshots for GIZMO concluding a commonality can not be made for certain.

explained via the inclusion of superbubble feedback in CHANGA, as it has been found to promote more efficient preventive outflows into the CGM that heat the CGM, impeding pristine gas accretion (in Paper IX.1).

The following two rows of panels show the hydrogen number density and the radial velocity respectively. Across all codes both properties are similar in their gas mass and volume behaviour. In the case of $n_{\rm H}$, all codes experience a steady decrease, starting with a little more than 10^{-2} cm^{-3} and finishing at $\sim 10^{-4.5}$ cm^{-3} in the dense regions[8], and a little less than 10^{-3} cm^{-3} and stopping at $\sim 10^{-5}$ cm^{-3} in the diffuse regions. One can also note that, as expected, the AMR codes and AREPO-T had slightly lower densities than the SPH codes and GIZMO, due to their ability to resolve more diffuse regions and the tendency of particle codes to be more clumpy (Agertz et al. 2007). Note that the decrease in density will partly be enhanced not only from the CGM heating up, but also from pseudo-evolution causing the CGM volume to increase, including more diffuse gas further out. For the radial velocities, the CGM of the different codes remain consistent throughout their evolution. Notably, the AMR codes seem to prefer in both the dense and diffuse regions a positive velocity, meaning the gas had a net outflow, while the rest experienced negative velocities in both regions, meaning net inflow. This coincides with the previously found results in Paper VI where ART-I and ENZO had much faster outflows than the particle codes. From those same results, however, it was shown that AREPO-T and GIZMO should be somewhere in-between, although here they were found to be more similar to the SPH codes.

The bottom row shows the bulk $t_{\rm cool}/t_{\rm ff}$, and comparing these with the temperature row, there is a clear similarity from their strong dependence. $t_{\rm cool}/t_{\rm ff}$ is further analysed and better visualised in Section 3.4, but initially it can be seen that most codes gradually increase over redshift, while GADGET-3 and GEAR have a rapid stability and remain just below the stability criterion $t_{\rm cool}/t_{\rm ff} = 1$ from $z = 4$ onwards. This redshift of $z \sim 4$ is important for all simulations as this approximately marks the beginning of the coalescence stage in the major merger at $z \sim 4.5$, which has significant implications for the stability of the CGM, more in Paper IX.1 and IX.2. These quick increases in $t_{\rm cool}/t_{\rm ff}$ for GADGET-3 and GEAR implies that the major merger greatly inhibited their cooling efficiency, consistent with delayed cooling breaking thermal equilibrium in gas, suppressing formation of cold, dense gas and thus inhibiting cooling.

3.3 Baryon budget and CGM Phases

While the total baryonic matter in the IGM, CGM, and ISM across these different codes were shown in Paper VI, the emphasis in this work was instead to compare it with the measured cosmic fraction via the baryon budget, defined as $(M_{\rm bar}/M_{\rm vir})/(\Omega_{\rm b}/\Omega_{\rm m})$[9], see Figure 3. It can be seen in the total baryon budget within $R_{\rm vir}$ that ENZO, GADGET-3, and GEAR were nearly complete, meaning equal to the cosmic fraction, with some mild fluctuations. ENZO and GADGET-3 kept above 90% for most of the time, and GEAR initially with a surplus at $\sim 110\%$, eventually lost enough to be within 5% by its final snapshot at $z = 0.3$. On the contrary, ART-I, AREPO-T, and GIZMO were consistently deficient, with the exception of a brief moment for AREPO-T, possibly due to the major merger at $z \sim 4.15$. The major merger event at this epoch caused most likely also all the sudden baryon budget increases seen in each code between $z = 4 - 3$. Two codes that were especially sensitive to this event was CHANGA and CHANGA-T which fluctuated around 1, like ENZO, GADGET-3, and GEAR, but experienced a significant increase in baryonic mass, peaking at $z \sim 3$. The similarity of this feature between the two CHANGA variants indicate that it is caused by their common implementation, although CHANGA showed a higher surplus of baryon budget meaning that inclusion of superbubble feedback promotes an increase in total gas from a merger.

The baryon budget in the CGM gas[10] also reveals differences between codes. All codes began at $z \sim 4.5$ by losing a significant amount of CGM baryons via gas accretion onto the ISM. The duration of this accretion varied strongly between codes, depending on their numerical implementation. CHANGA-T, GADGET-3, and GEAR, all SPH codes, ceased at $z \sim 4$ after which reached a plateau, and subsequently recovered some baryons before their final snapshot. The final SPH code, CHANGA, experienced a unique behaviour where the CGM gas was left suspended until $z \sim 3$ before rapidly accreting onto the central galaxy. This has been shown in Appendix C in Paper IX.1 to be caused by a delayed merger-induced starburst due to the superbubble implementation. ART-I, ENZO, AREPO-T, and GIZMO instead continued until $z \sim 2$ ($z \sim 2.8$ for GIZMO) before reaching a minimum and recovering about 10 – 15%. From the mixture of feedback models in the two major groups of CGM gas loss longevity, how smoothly the CGM loses its baryons seems to be a result of numerical implementation rather than how stellar feedback was implemented. While SPH codes experienced a sharp loss of baryons, the AMR, MM, and MF codes prolonged this process more smoothly. By $z \sim 0.3$, all relevant codes were found to be seemingly stable at a budget between 40% - 15% inside the CGM, except GADGET-3 closer to 60%.

In order to probe the multiphase evolution within the CGM, the CGM baryon budget was divided up into a cold ($T < 2 \cdot 10^4$ K), warm ($2 \cdot 10^4 < T < 3 \cdot 10^5$ K), and hot ($T > 3 \cdot 10^5$ K) component[11], see Figure 4. In addition, to more clearly compare just the transition redshift between dominant thermal phases, at the loss of baryon budget contribution, see Figure 5. All codes, except GADGET-3, show an initial, $z \sim 5$, dominant cold gas contribution of ~ 30 to $\sim 50\%$. GADGET-3 had instead a much hotter CGM in the earlier epoch, with roughly equal contribution of cold, warm, and hot gas, each at $\sim 20\%$. GIZMO had relatively prominent warm gas component, compared to other codes, which was similar in contribution to its cold phase both at $\sim 30\%$, with a hot component around $\sim 10\%$. Unlike other codes that had a fairly consistent warm gas contribution of $\sim 10\%$, GADGET-3 and GIZMO showed a decreasing trend, although by $z \sim 2$ GADGET-3 only lost $\sim 10\%$ while and GIZMO lost $\sim 20\%$. This difference can be explained with their different feedback schemes, as GADGET-3 had implemented delayed cooling which puts gas into a thermal non-equilibrium, suppressing cooling and thus transition for the warm gas into cold. In addition, it was noted in Paper IX.1 that both GADGET-3 and GIZMO experienced

[8] For the codes that reach $z = 0$, although they have similar magnitudes as other codes at their final redshift.

[9] Note that the definition of the virial radius is done via only the dark matter (see e.g. Paper III), and will hence be underestimated in this definition as more than just the dark matter is considered in the definition of $M_{\rm vir}$. Alternative definitions have been tested but yield very little difference and thus this one is kept to ease comparison with other work.

[10] Note that, although the CGM incorporates a stellar component, the contribution is expected to be negligible.

[11] These temperature cuts were chosen from the minimum cooling efficiency temperature $10^{4.3}$ K from Liang & Remming (2020) to the peak cooling efficiency temperature $\sim 3 \cdot 10^5$ K (Gnat & Sternberg 2007; Das et al. 2021).

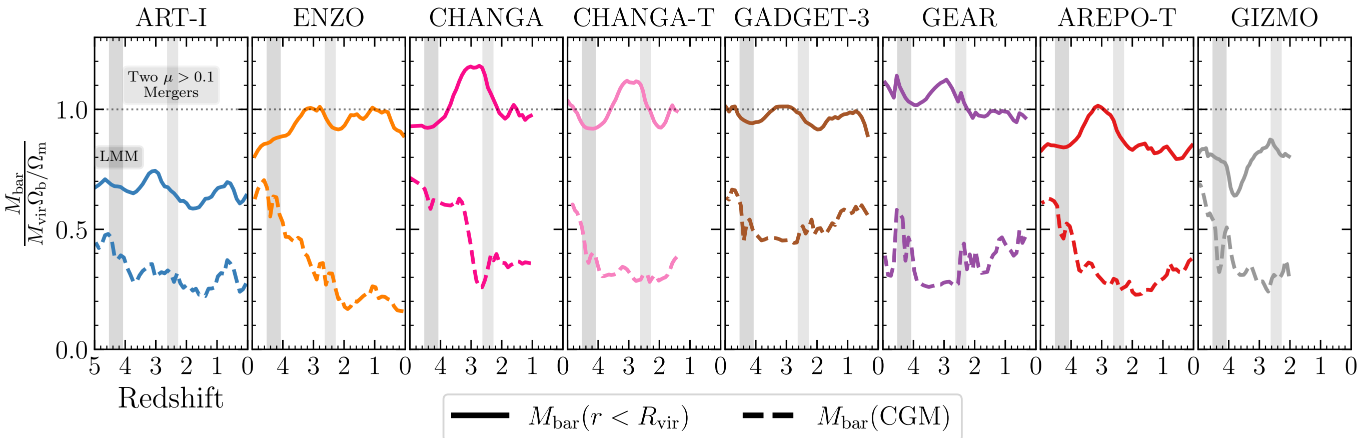

Figure 3. Ratio between the baryonic mass in both the entire galaxy $M_{bar}(r < R_{vir})$, including stars and gas, and in the CGM $M_{gas}(CGM)$, which includes only gas within the CGM boundaries, taken over the virial mass relative to the expected baryonic to total mass ratio of the Universe Ω_b/Ω_m. Note that the grey-shaded regions indicate the approximate time for the last major merger (LLM) at $z \sim 4.5$, see Paper IX.1 and IX.2, and two minor mergers at $z \sim 2.5$ which were noted in Paper IV.

significant starbursts at $z \sim 5.6$, resulting in intense feedback-driven outflows into their respective CGM, providing the early high contributions of warm and hot gas seen in Figure4. All SPH codes and AREPO-T (not GIZMO due to its much shorter run) had by their final snapshot a clear dominant hot gas phase with $\sim 30-50\%$ of the baryon budget. ART-I and ENZO, both of which had the lowest total CGM budget, had also much lower hot gas contribution at $\sim 15\%$. Interestingly, despite its low total budget, ART-I still had a very similar warm gas contribution at $\sim 10\%$ like all other codes, excluding ENZO with closer to $\sim 4\%$. The SPH codes, unlike the others, did not show an intermediate epoch of warm gas dominating, and instead transitioned directly from a cold to a hot CGM. This coincides with the lack of warm gas in Figure 2, due to the inability of SPH codes to resolve low density gas (also see Figure 8 in Paper VI).

All codes had at certain times missing baryons within R_{vir} and in order to see where these baryons have gone, the baryon closure radius R_c[12] (Ayromlou et al. 2023) was used. In Figure 6, R_c is shown for each code across their respective available redshift, starting from $z = 5$. Generally, the shape of the curve from each code are similar. They all show an initial broad peak, with a maximum at about $z \sim 4$, followed by a steady decrease, reaching a minimum at $z \sim 3$, but then recovering similar values or more by $z \sim 2$. The first two features, the peaks and troughs, and their timing differences are related to the major merger that occurred at $z \sim 4.5$, see Paper IX.1 and IX.2 for further details. Beyond that, the curves seem to fluctuate but not experience any drastic changes until $z = 1$ where only ART-I and AREPO-T experienced a significant decrease of $\sim 0.5 R_c/R_{vir}$, before recovering again. This has been verified to caused by a minor merger. After $z \sim 0.5$, ART-I and ENZO both increased significantly in their R_c/R_{vir}, while AREPO-T remains mostly constant. This follows from the previously found result in Paper VI that the AMR codes, especially ART-I, had much more efficient outflows that could eject the missing baryons further out, and ART-I and ENZO established a less massive hot corona, see Figure 4, which would be less efficient at preventing outflows. Comparing the strength of the features, the two thermal+kinetic codes ART-I and GIZMO have significant initial peaks, increasing R_c by $\approx 0.5R_{vir}$. The codes with delayed cooling, GEAR and GADGET-3, have R_c closer to $\approx 0.2R_{vir}$, with the remaining pure thermal and thermal+superbubble codes varying between these two extremes. The pure thermal codes are also seen to have similar initial peaks during the major merger, although deviate post-merger with AREPO-T maintaining stronger outflows, as was shown in Paper VI.

In order to more easily both see the radial distribution of the baryon budget, it was instead plotted against physical radius at certain redshift $z = 5, 4, 3, 2, 1,$ and 0.3 in Figure 7. The codes initially were in good agreement, but with time they split up into more distinct groups, with ART-I quickly becoming an outlier. By $z = 0.3$, GADGET-3 and GEAR end up with a very similar baryon budget distribution along R with an almost sigmoid curve, reinforcing the idea that they had weak feedback that is unable to eject baryons very far. ART-I, ENZO, and AREPO-T, on the other hand, show instead linear radial profiles. ART-I had the steepest increase with R, followed by AREPO-T, and finally ENZO. These differences also consistent with the AMR codes and AREPO-T having much more efficient outflows and thus are capable of expelling their baryons far beyond R_{vir}, explaining the linear function, while the SPH codes are much more limited by their weaker outflows and eventually their baryons will not be carried further and the curves flatten out. The high concentration in the centre for ENZO has also been noted in past AGORA work, see Paper VI and Paper VIII. It was caused by ENZO's strong pure thermal feedback suppressing early star formation, but subsequently allowing a much higher later star formation rate, resulting in galactic stellar mass (total mass of stars within $0.15R_{vir}$) dominating over the total CGM mass.

3.4 Radial Evolution of Gas Properties

In order to get an overview of the radial distribution of some CGM properties, temperature, relative metallicity, and t_{cool}/t_{ff}, their mass-weighted medians were binned, both in radius and in z, see Figure 8. Note that these plots are biased to the dense gas by taking the mass-weighted median. All codes show the trajectory and properties of the two minor (mass ratio > 0.1) merger at $z \sim 2.2$ as trails of

[12] Defined as the radius from the galactic centre that creates a spherical volume which encloses enough baryonic mass such that $M_{bar}/M_{vir} = \Omega_b/\Omega_m$.

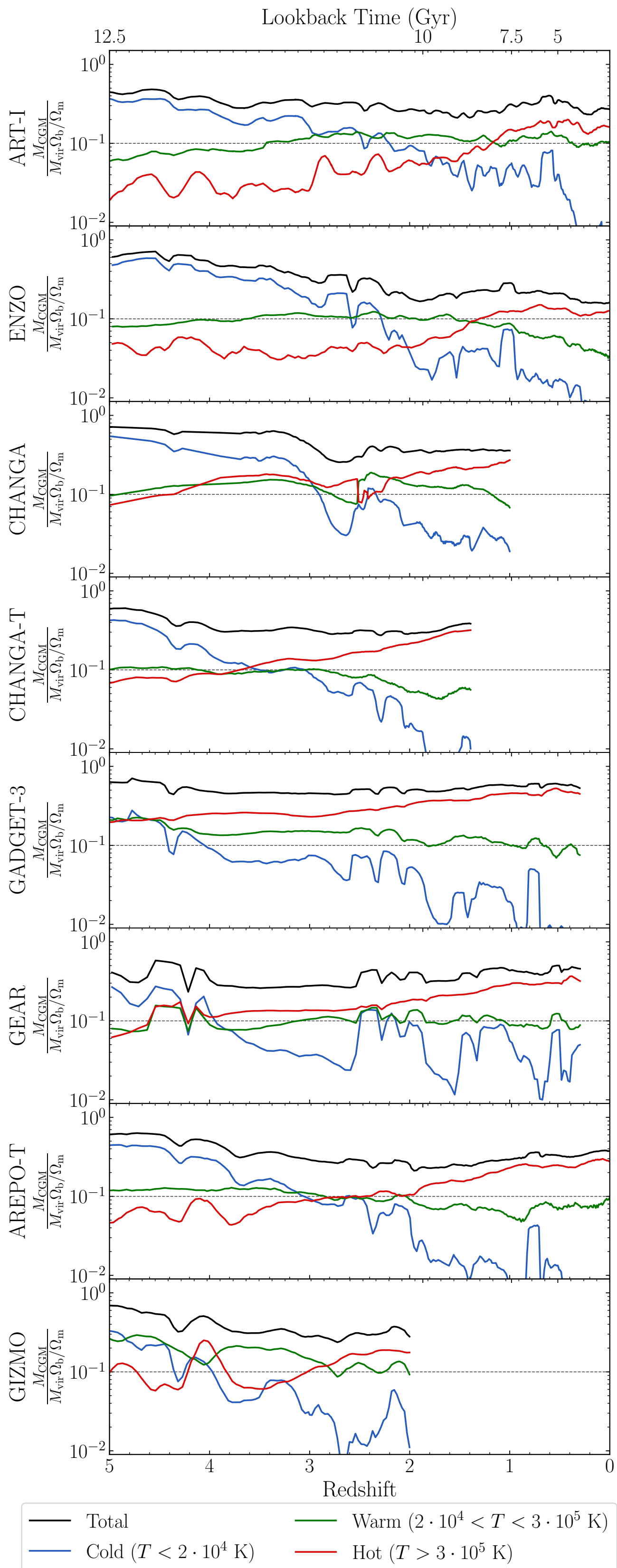

Figure 4. The CGM gas mass $M_{\rm gas}$ over the virial mass $M_{\rm vir}$ relative to the expected baryonic to total mass ratio of the Universe Ω_b/Ω_m, where the CGM gas has been divided up into three different temperature ranges: cold ($T < 2 \cdot 10^4$ K); warm ($2 \cdot 10^4 \leq T \leq 3 \cdot 10^5$ K); and finally hot ($T > 3 \cdot 10^5$ K).

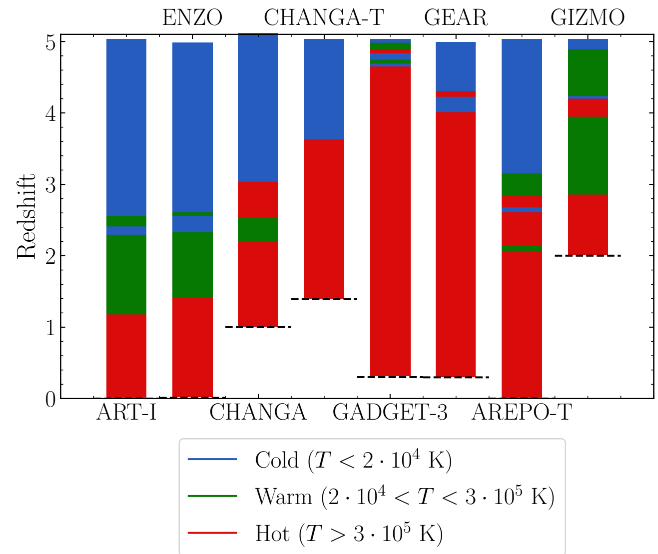

Figure 5. The dominating CGM gas phase in Figure 4, either cold ($T < 2 \cdot 10^4$ K); warm ($2 \cdot 10^4 \leq T \leq 3 \cdot 10^5$ K); and finally hot ($T > 3 \cdot 10^5$ K), at each redshift for each code. Note the black dashed lines indicate when each code runs out of snapshots, see Table 1 for more details.

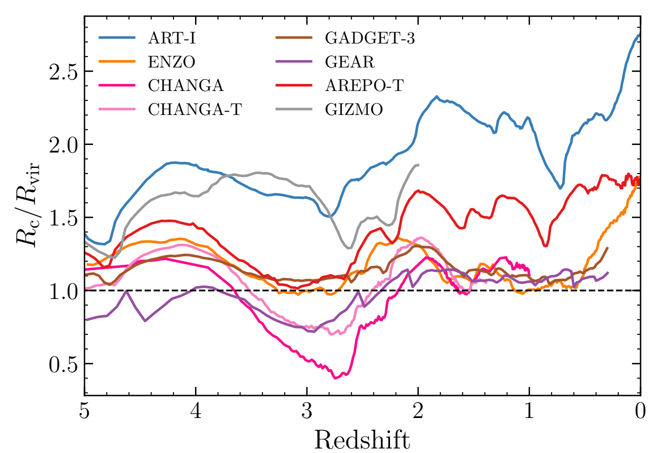

Figure 6. The baryon closure radius $R_{\rm c}$ relative to the virial radius $R_{\rm vir}$ at all available snapshots with $z \leq 5$.

cold, metal-rich, and dynamically unstable gas. In the $t_{\rm cool}/t_{\rm ff}$ plots, these minor mergers, together with all merging satellites, differed in contrast to their surroundings via a distinct lower $t_{\rm cool}/t_{\rm ff}$, while in ENZO and AREPO-T they were much less obvious. All codes showed similar gas temperatures and metallicities evolutions which implies that ENZO and AREPO-T must instead differ in density. It was found in Paper VII, that both ENZO and AREPO-T showed very significant quenching of satellites compared to GADGET-3 and GEAR, due to their weaker restoring pressure, and thus lower density, caused by their more efficient outflows. GADGET-3 and GEAR, both using delayed cooling, showed higher temperatures and low metallicity within the CGM at the earlier times. From this it becomes clear that the metal-rich gas was not lost into the IGM but rather never left the ISM. This is most likely due to their weak ejective feedback, although GEAR eventually experiences a significant outflow of metals,

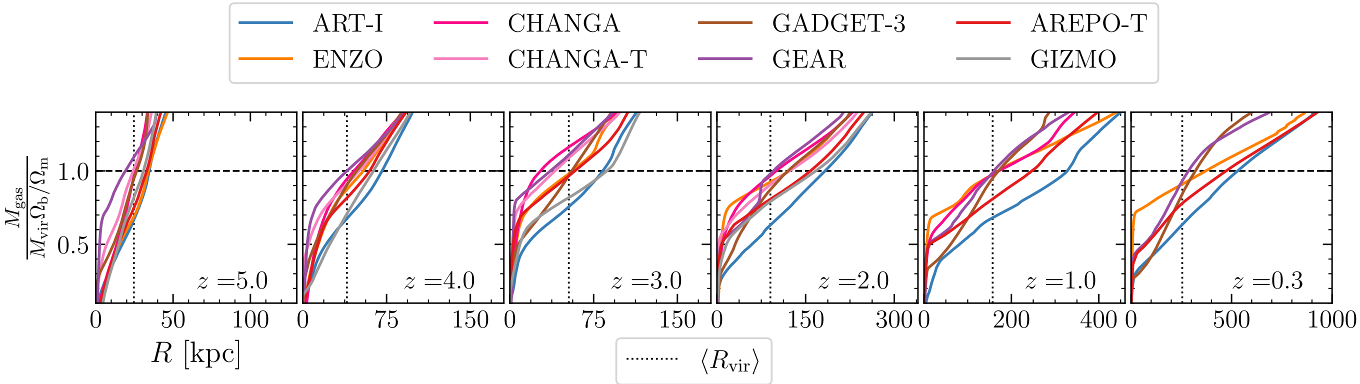

Figure 7. The baryonic mass fraction over the cosmic mass fraction plotted against radius, taken at $z = 5$, 4, 3, and 2 for each simulation, and continued to $z = 1$ and 0.3 for those that reach these redshift. Note that the radius range generally increases with decreasing redshift. In addition, the dashed line indicates where the baryon budget is equal to 1, and thus the radius at that point is the baryon closure radius $R_{\rm c}$, and the dotted line is the mean virial radius between all codes.

possibly caused by the major merger at this time[13]. GIZMO showed a similar lack of metallicity, but did not have enough time to experience a possible eruption of metals as GEAR did. The other codes were capable of expelling metal-rich gas well within the CGM, with ENZO, AREPO-T, and especially ART-I ejecting metals far past $R_{\rm vir}$ in the earlier times.

3.5 Virialisation of the CGM

By sampling certain selected shells around the main galaxy, the virialisation could be examined in more detail than Figure 2 or Figure 8, as was done in Figure 9. The top two rows show the history of the mass-weighted $t_{\rm cool}/t_{\rm ff}$ median following the edges of the CGM definition used in this work. An interesting feature in the inner CGM is ENZO, GEAR, and AREPO-T, all start off above $t_{\rm cool}/t_{\rm ff} = 1$ at $z \sim 5$, but then destabilise at $z \sim 4.5$. This implies that they initially had some dominant central feature that prevented effective cooling. Following the $R_{\rm vir}$ CGM definition, each code, with the exception of CHANGA-T, show an outside-in virialisation, where the shell at $R_{\rm vir}$ passes $t_{\rm cool}/t_{\rm ff} > 1$ before $0.2R_{\rm vir}$. This is especially obvious for ART-I which showed a virialisation at $z_{\rm R_{vir}} \approx 1.8$ and $z_{\rm 0.2R_{vir}} \approx 0.4$.

The next four rows of Figure 9 instead show the mass-weighted median of $t_{\rm cool}/t_{\rm ff}$ in shells with fixed radii 50, 100, 150, and finally 200 kpc, circumventing problems from pseudo-evolution. Certain codes are seen to reach the virialisation condition $t_{\rm cool}/t_{\rm ff} > 1$ and increase very quickly, see e.g. CHANGA at 50 kpc. Others instead linger just above $t_{\rm cool}/t_{\rm ff} = 1$ for a prolonged period, seemingly amplified with radial distance, most consistently for ART-I that never reaches the $t_{\rm cool}/t_{\rm ff} \gtrsim 10$. GADGET-3 at 50 kpc, and ENZO at 200 kpc both show a prolonged plateau instead just beneath $t_{\rm cool}/t_{\rm ff} = 1$, not able to reach quasi-equilibrium until later. For ENZO this can be explained from Figure 8, which shows an extended structure amidst stable gas that disrupted virialisation. The source is most likely from the visible slightly colder and metal-rich inflows of merging satellites that strip their gas, disrupting virialisation. For GADGET-3, it was caused by the inner CGM being heated, most likely by feedback, creating a region of higher $t_{\rm cool}/t_{\rm ff}$, but not enough to reach quasi-equilibrium.

In order to see where each radial shell virialised, the points where $t_{\rm cool}/t_{\rm ff} = 1$ were collected in Figure 10, together with an approximate uncertainty from the borders of the shaded area at $t_{\rm cool}/t_{\rm ff} = 0.75$ and $t_{\rm cool}/t_{\rm ff} = 2$. The differences between codes can be seen to decrease depending on radial distance. The highest, although for most not significant, disparity was found in the inner CGM, while the majority of codes virialised at a similar epoch in the outer regions. In the inner regions, the codes can be divided up into four groups, ordered by descending virialisation time: AREPO-T and GIZMO at $z \sim 3$, followed by CHANGA-T, GEAR, and GADGET-3 at $z \sim 2.5$; then ENZO and CHANGA at $z \sim 2.1$, and finally ART-I at $z \sim 1.6$. Further out, all codes, except ENZO CHANGA, seem to gradually gather until eventually at 150 kpc they all convened at $z = 2.5 \pm 0.2$, and at 200 kpc they fell between $z = 2.6 \pm 0.3$. ENZO and CHANGA instead followed their own tracks at slightly lower redshift, $z \sim 1.8$ and $z \sim 2.1$ respectively. CHANGA also experienced a sharp drop at 200 kpc as it was disturbed by merging satellites. A striking similarity between all codes, except ART-I, is the relatively low variation of virialisation redshift across shell radii, implying a scenario of halo wide virialisation where these codes stabilised across their haloes, nearly independent on radius.

4 DISCUSSION

This section compiles, reiterates, and further discusses certain points made in the results.

4.1 Impact of Stellar Feedback and Numerical Implementation on Metal and Baryonic Distribution

In order to constrain the role of stellar feedback in Milky Way-mass galaxies, several different feedback models were compared, all with accompanying differences of implementation. We will now show that the choice of stellar feedback model and code implementation is vital for the efficiency of metal and baryon regulation, and establishing the CGM multiphase.

All grid codes and AREPO-T were relatively efficient at ejecting metals beyond $R_{\rm vir}$, compared to the other codes which instead kept most of their metals bound. The AMR codes, ART-I and ENZO differed substantially, however, on the amount of missing baryons. ENZO lost only about 10% of its baryon budget while ART-I lost closer to $\sim 30 - 40\%$, with AREPO-T somewhere in between at $\sim$

[13] This will be checked in future AGORA work.

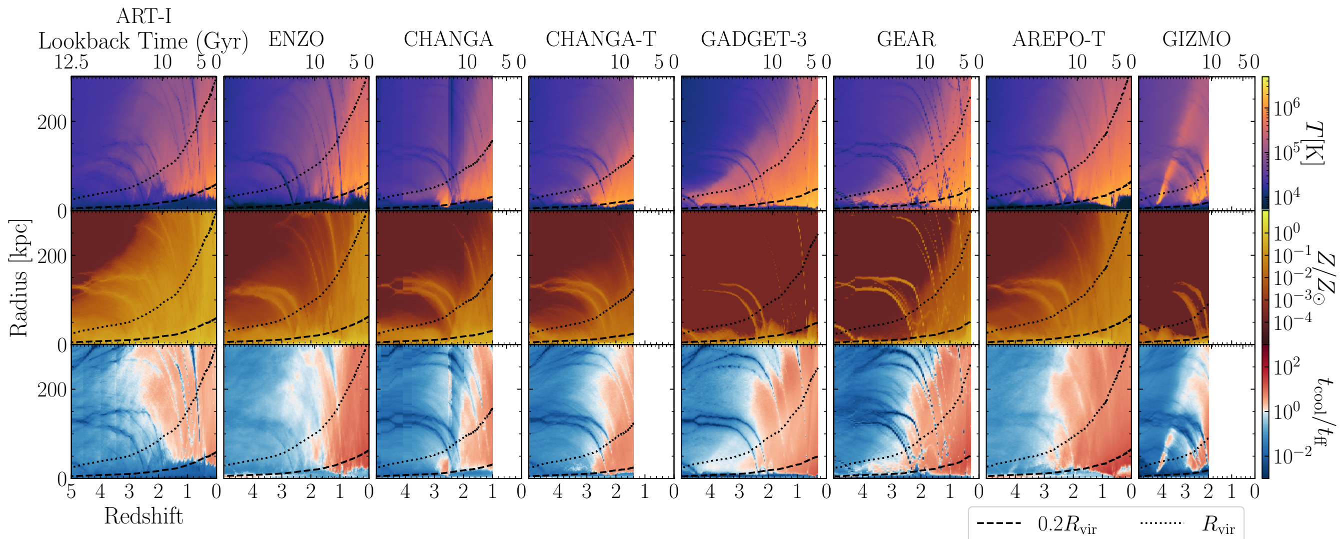

Figure 8. The radial mass-weighted medians of the temperature, metallicity (relative to $Z_\odot$), and t_{cool}/t_{ff} from each involved code across all their respective available z. Note that the dashed and dotted lines indicate the inner and outer CGM boundaries respectively.

15 – 20%. This means that the inclusion of kinetic feedback supports more efficient outflows of baryons, especially after the major merger at $z \sim 4.5$, which can be confirmed with the closure radius of GIZMO. Although, despite GIZMO managing to expel significant gas, a higher metallicity did not appear beyond R_{vir} in Figure 8. We hypothesise that it is caused by GIZMO pushing out much of its pristine gas that has not mixed well with the newly enriched gas from the starburst. Despite both ENZO and AREPO-T having pure energetic thermal feedback, ENZO is shown here to be less ejective, suggesting that the implementation in AREPO-T is generally better at baryon regulation than AMR. Although, by $z = 0$ they had the same closure radius, see Figure 6, despite their final total baryon budget differing by $\sim 5\%$. While AREPO-T managed to sustain a significant hot dominated CGM (baryon budget of $\sim 30\%$), which would prevent feedback-driven outflows, ENZO could not and hence, like ART-I, experienced a burst of baryon ejection at $z \lesssim 0.6$. Despite this sudden baryon loss, comparing even the most ejective feedback model among CosmoRun suite, in ART-I, the closure radius was much lower than other those shown in Ayromlou et al. (2023), which instead found for Milky Way-mass galaxies $\sim 10 R_c/R_{200c}$. The SPH codes regulated their total and CGM baryons similarly, independent on their feedback implementation, with a closure radius within $1.2 R_{vir}$ by $z \gtrsim 1.6$.

The gas phases between all codes were found to be in the same sequence at the later times, with the hot gas dominating, followed by the warm, and finally the cold gas. This is consistent with current beliefs, where it is suspected that a significant fraction of the baryon budget in galaxies is stored in a hot component in the CGM that is difficult to observe (see e.g. Figure 2 in Chen & Zahedy 2026). The relative contributions of each phase throughout their evolution, however, differed strongly between most codes. Interestingly, most codes developed a relatively stable intermediate warm gas phase, remaining stable at $\sim 10\%$ of the CGM baryon budget. This was true for both ART-I and GADGET-3, despite having a $\sim 30\%$ difference in total CGM baryon budget. The simulations using pure thermal feedback, however, generally predict more significant relative deficiencies of warm gas despite a wide variety of both total and hot CGM baryon budget. This coincides with Paper IX.1, where the gas in thermal-only models could keep cooling, converting warm gas in the CGM to cold gas in the ISM, long after the major merger at $z \sim 4.5$.

The SPH, MM, and MF codes, unlike the AMR codes, all had certain redshift where the cold, warm, and hot gas were all more or less equal. Although this occurred at very different moments and at varying fractions, a possible explanation is the ability for AMR to resolve lower density gas, meaning transitions between phases are smoother and not as coupled. While keeping similar hot and warm gas contributions, GEAR showed a stronger cold gas component than other codes. This is in contrast with results from (Rey et al. 2025) where they showed that delayed cooling causes the CGM to be primarily populated by hot, diffuse gas.

4.2 Differences and Similarities for CGM Virialisation

Stellar feedback not only regulates baryons but also provides the CGM with additional energy and possibly momentum, both of which affect its dynamical stability versus cooling. The following part will show that neither stellar feedback model nor code implementation seem to have a significant effect on the virialisation of the outer halo, and minimal effect on the inner CGM, with some exceptions.

The difference between t_{cool}/t_{ff} within the CGM definition and from the fixed shells reveals clear differences, possibly an effect of pseudo-evolution. While the CGM definition predicts, albeit weakly for most codes, the outside-in behaviour shown by (Stern et al. 2020), this does not reflect the extended halo. Instead, most codes, with the exception of ART-I, experienced a halo wide virialisation at redshift $z \sim 2$ to $z \sim 3$, earlier than predicted by virial shocks (Birnboim & Dekel 2003). This suggests a third possible CGM virialisation scenario to the two current alternatives of either inside-out or outside-in. The clear difference to the outside-in scenario is that these models had significantly slower and less efficient baryon regulation, given the exception of ART-I, suggesting a correlation.

While the outer regions showed fractional virialisation redshift disparity for most codes, especially at 150 kpc, the inner CGM offered more clear groups of codes. These slight differences are most likely caused by the different stellar feedback models. Alternatively, as can be seen in Figure 8, sensitivity to mergers, as, for example, CHANGA shows an earlier epoch of inner CGM virilisation at $z \sim 2.7$, but

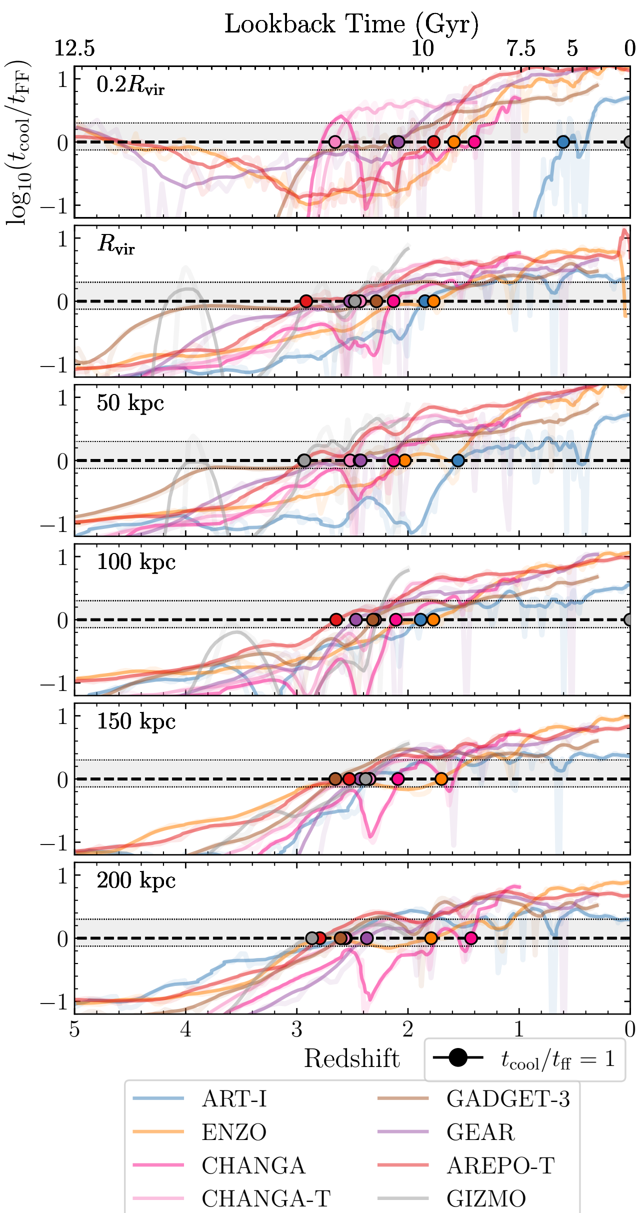

Figure 9. Mass-weighted medians of $\log_{10}(t_{\rm cool}/t_{\rm ff})$ in shells located at the boundaries of the CGM and at four different fixed radii, each with a width of 4 kpc. Note that the points where the $\log_{10}(t_{\rm cool}/t_{\rm ff})$ lines first cross and stay above 1 for a time longer than 500 Myr (DeFelippis et al. 2026).

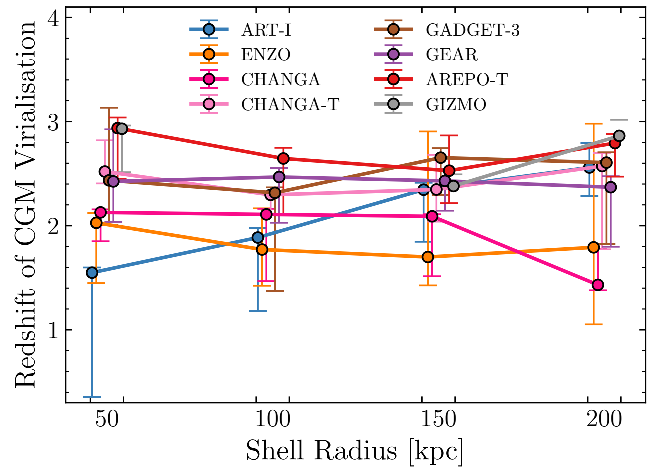

Figure 10. The fixed shell radii from Figure 9 plotted with their respective redshift where they cross the three indicated thresholds. Note that $t_{\rm cool}/t_{\rm ff} = 1$ is the central marker and the lower and upper thresholds are used to approximate uncertainties, with lower uncertainty meaning sharper transition i.e. more obvious stability.

was disturbed by the last major merger, delaying spherically mass-weighted virialisation.

4.3 Limitations & Caveats

Even though these simulations are zoom-in, the numerical resolution was limited and not low enough to resolve the small-scale processes that are no doubt important. This is an issue for all current cosmological simulations, but the inaccuracies are lessened by using carefully constructed sub-grid models (Vogelsberger et al. 2020). For an overview of the mass distribution based on resolution see Figure 1 in Paper VI.

An additional constraint was the lack of snapshots at lower redshift for some of the codes included, see Table 1. But because of this difference, the results from some codes can not be as fairly examined and there might be hidden effects that would occur at lower redshift. Therefore, in the analysis, the behaviour of each code that did not reach lower redshift was made more carefully, and comparison with the others were only made up until either of their final redshift. The power of comparison projects comes from the amount of simulations that are being compared, and thus less clear conclusions can be made at these later times. This could have been an issue for the baryonic fractions, as they are very dependent on virial radius. For the virialisation part, most codes exhibited their desired behaviours before $z = 2$, meaning all codes could capture it. Although for GIZMO it was not as robust as certain unexpected phenomena at later times could be conceivable.

An important approximation is the use of $t_{\rm cool}/t_{\rm ff}$ to quantify the virialisation of the CGM. Despite using the mass-weighted median, a statistic that is usually fairly robust, it can be seen that $t_{\rm cool}/t_{\rm ff}$ still fluctuated quite substantially, most obvious in Figure 9. When comparing with Figure 8 it becomes evident that $t_{\rm cool}/t_{\rm ff}$ is very sensitive to satellite mergers, the dark blue streaks that are clear in most codes, except ENZO and AREPO-T. Because of this, it must be noted that the definition used here for the virialisation is more focused on marking the onset stability, when the majority of the mass reaches a quasi-equilibrium. However, other work, such as Stern et al. (2021), used similar definitions and thus should experience the same sensitivity, meaning comparisons between these works are fair. There are many alternative methods, although many of them closely linked, for quantifying this, e.g. entropy (Keller et al. 2020) or Mach number (Stern et al. 2020) but these are beyond the scope of this work and could possibly be interesting to investigate in the future.

5 SUMMARY AND CONCLUSIONS

In this paper, the CGM evolution and virialisation was presented from eight state-of-the-art hydrodynamical codes in the AGORA CosmoRun suite of cosmological zoom-in simulations of Milky Way-mass galaxies. Each code differed both in their hydrodynamic solving and in their stellar feedback scheme, and by comparing their CGM over time, the significance of these differences could be shown and analysed. The key results of this work are summarized here:

- A strong metallicity disparity was found in the CGM related to their different feedback models and implementation. SPH and preventive models predict less metal-rich gas while AMR and ejective feedback had a higher metallicity.
- Most codes could close their baryon budget close to $R_{\rm vir}$, and all codes predicted CGM baryon mass fraction of $\sim 20-50\%$ relative to the expected cosmic baryon fraction.
- Comparing the thermal CGM multiphase in each simulation showed a wide variety of evolutions. Most codes showed a similar warm ($2 \cdot 10^4 < T < 3 \cdot 10^5$ K) gas contribution of $\sim 10\%$, except thermal-only codes with a proclivity for $\sim 5\%$. Comparing general feedback differences showed that GADGET-3 with strong preventive feedback established a hot corona already at $z \sim 4$, while ART-I with strong ejective feedback had a dominant hot component much later at $z < 1.2$.
- The virialisation of the inner CGM varied enough between codes to form distinct groups: AREPO-T and GIZMO at $z \sim 3$; CHANGA-T, GEAR, and GADGET-3 at $z \sim 2.5$; ENZO and CHANGA at $z \sim 2.1$; and finally ART-I at $z \sim 1.6$. This redshift disparity greatly decreased for all codes, except ENZO and CHANGA, with radial distance and by 150 kpc and 200 kpc the common redshift was 2.5 ± 0.2 and 2.6 ± 0.3 respectively.
- In contrast to the inside-out or outside-in scenarios for CGM virialisation, this work found a third option of halo wide virialisation at the same epoch. This alternative could arise from inclusion of stellar feedback but with insufficient regulation of baryons, as only the code with significant missing baryons, ART-I, showed instead outside-in virialisation.

These results reveal that the inclusion of stellar feedback does not always provide the outside-in virialisation predicted by Stern et al. (2019, 2020). Instead, the numerical implementation and feedback parameters have a significant effect on the multiphase gas, with certain settings allowing for a surprisingly early hot CGM, already at $z \sim 5$. Whether this was possible due to the major merger at this time is yet not clear. Regardless, recent observations have shown galactic disks settling much earlier than our current models predict (Semenov 2026). One theorised option that would allow this, proposed in e.g. Stern et al. (2021), is if the hot corona is onset much earlier. This would allow the CGM to transition into stable hot accretion and potentially mitigate the effect of strong disturbances, such as minor mergers, both of which could facilitate the settling of the disk.

While the simulations used in this work include stellar feedback, they do not include all known feedback sources from e.g. active galactic nuclei (AGN), magnetic fields, and cosmic rays. It is a future desire and ongoing effort of the AGORA Collaboration to rerun these simulation codes, together with new ones, including further baryonic physics that are important for galaxy formation, and higher resolution.

ACKNOWLEDGEMENTS

Acknowledgement will be written before submission in accordance to the AGORA Collaboration requirements.

DATA AVAILABILITY

The data underlying this article were accessed from the AGORA FlatHUB. The derived data generated in this research will be shared on reasonable request to the corresponding author.

REFERENCES

Agertz O., et al., 2007, MNRAS, 380, 963
Ayromlou M., Nelson D., Pillepich A., 2023, MNRAS, 524, 5391
Birnboim Y., Dekel A., 2003, MNRAS, 345, 349
Bregman J. N., Hodges-Kluck E., Qu Z., Pratt C., Li J.-T., Yun Y., 2022, ApJ, 928, 14
Bryan G. L., Norman M. L., 1998, ApJ, 495, 80
Cantalupo S., et al., 2019, MNRAS, 483, 5188
Chen H.-W., Zahedy F. S., 2026, in , Encyclopedia of Astrophysics. Elsevier, pp 370–400, doi:10.1016/B978-0-443-21439-4.00059-6
Das S., Mathur S., Gupta A., Nicastro F., Krongold Y., Null C., 2019, ApJ, 885, 108
Das S., Mathur S., Gupta A., 2020, ApJ, 897, 63
Das S., Mathur S., Gupta A., Krongold Y., 2021, ApJ, 918, 83
DeFelippis D., Genel S., Bryan G. L., 2026, ApJ, 1002, 203
Dekel A., Birnboim Y., 2006, MNRAS, 368, 2
Faucher-Giguère C.-A., Oh S. P., 2023, ARA&A, 61, 131
Feldmann R., Bieri R., 2025, Cosmological Simulations of Galaxies (arXiv:2507.08925)
Ferland G. J., et al., 2013, Rev. Mex. Astron. Astrofis., 49, 137
Ferland G. J., et al., 2023, The 2017 Release of Cloudy (arXiv:1705.10877)
Fielding D., Quataert E., McCourt M., Thompson T. A., 2017, MNRAS, 466, 3810
Gnat O., Sternberg A., 2007, ApJS, 168, 213
Gupta A., Mathur S., Krongold Y., Nicastro F., Galeazzi M., 2012, ApJ, 756, L8
Hafen Z., et al., 2019, MNRAS, 488, 1248
Jung M., et al., 2025, ApJ, 994, 245
Kacprzak G. G., et al., 2025, Publ. Astron. Soc. Australia, 42, e128
Keller B. W., Wadsley J., Benincasa S. M., Couchman H. M. P., 2014, MNRAS, 442, 3013
Keller B. W., Kruijssen J. M. D., Wadsley J. W., 2020, MNRAS, 493, 2149
Lehner N., et al., 2020a, in American Astronomical Society Meeting Abstracts #235. p. 430.04
Lehner N., et al., 2020b, ApJ, 900, 9
Liang C. J., Remming I., 2020, MNRAS, 491, 5056
Liang C. J., Kravtsov A. V., Agertz O., 2016, MNRAS, 458, 1164
McClain R. L., Mathur S., Das S., Krongold Y., Gupta A., 2024, MNRAS, 527, 5093
McGaugh S. S., Schombert J. M., de Blok W. J. G., Zagursky M. J., 2010, ApJ, 708, L14
McGaugh S. S., Mistele T., Duey F., Haubner K., Lelli F., Schombert J. M., Li P., 2026, ApJ, 1001, 65
Mitchell P. D., Blaizot J., Devriendt J., Kimm T., Michel-Dansac L., Rosdahl J., Slyz A., 2017, MNRAS, 474, 4279
Mo H., van den Bosch F. C., White S., 2010, Galaxy Formation and Evolution, doi:10.1017/CBO9780511807244.
Münch G., Zirin H., 1961, ApJ, 133, 11
Nicastro F., et al., 2023, ApJ, 955, L21
Peroux C., Nelson D., 2024, The Multi-Scale Multi-Phase Circumgalactic Medium: Observed and Simulated (arXiv:2411.07988)
Putman M. E., Peek J. E. G., Joung M. R., 2012, ARA&A, 50, 491
Rees M. J., Ostriker J. P., 1977, MNRAS, 179, 541
Rey M., Blaizot J., Kimm T., Rosdahl J., Michel-Dansac L., 2025, MNRAS, 543, 12
Rintoul T. A., van de Voort F., Hannington A. T., Pakmor R., Bieri R., Werhahn M., Talbot R. Y., 2025, MNRAS, 543, 4321
Roca-Fàbrega S., et al., 2021, ApJ, 917, 64
Roca-Fàbrega S., et al., 2024, ApJ, 968, 125
Rodríguez-Cardoso R., et al., 2025, A&A, 698, A303

Ruszkowski M., Pfrommer C., 2023, A&ARv, 31, 4
Semenov V. A., 2026, How Do Disk Galaxies Form? (arXiv:2602.04950)
Shen S., Madau P., Guedes J., Mayer L., Prochaska J. X., Wadsley J., 2013, ApJ, 765, 89
Silk J., 1977, ApJ, 211, 638
Smith B. D., et al., 2017, MNRAS, 466, 2217
Somerville R. S., Davé R., 2015, ARA&A, 53, 51
Spitzer Jr. L., 1956, ApJ, 124, 20
Stern J., Fielding D., Faucher-Giguère C.-A., Quataert E., 2019, MNRAS, 488, 2549
Stern J., Fielding D., Faucher-Giguère C.-A., Quataert E., 2020, MNRAS, 492, 6042
Stern J., et al., 2021, ApJ, 911, 88
Strawn C., et al., 2024, ApJ, 962, 29
Tumlinson J., et al., 2011, Science, 334, 948
Tumlinson J., et al., 2013, ApJ, 777, 59
Tumlinson J., Peeples M. S., Werk J. K., 2017, ARA&A, 55, 389–432
Vogelsberger M., Marinacci F., Torrey P., Puchwein E., 2020, Nature Reviews Physics, 2, 42
Werk J. K., et al., 2016, ApJ, 833, 54
White S. D. M., Frenk C. S., 1991, ApJ, 379, 52
White S. D. M., Rees M. J., 1978, MNRAS, 183, 341
Woo J., et al., 2013, MNRAS, 428, 3306
Woods R. M., Wadsley J., Couchman H. M. P., Stinson G., Shen S., 2014, MNRAS, 442, 732
Wright R. J., Somerville R. S., Lagos C. d. P., Schaller M., Davé R., Anglés-Alcázar D., Genel S., 2024, MNRAS, 532, 3417
Zhang, X. et al., 2026, A&A, 709, A72
Zhang Y., Liu R.-Y., Li H., Shao S., Yan H., Wang X.-Y., 2021, ApJ, 911, 58
van de Voort F., Schaye J., 2013, MNRAS, 430, 2688

This paper has been typeset from a TEX/LATEX file prepared by the author.

Chapter 5

Conclusions and Outlook

This thesis has analysed and compared the evolution of the circumgalactic medium (CGM) in a suite of eight state-of-the-art cosmological simulations, all provided by the AGORA Collaboration (same ones used in Roca-Fàbrega et al., 2021, 2024). Each simulation were run using the same initial conditions, heating/cooling method, and star formation conditions but they varied in numerical implementation and stellar feedback prescription. This was done in order to see whether these differences could be shown and distinguished by comparing the formation and evolution of their galaxies, more specifically their CGM.

It was found that the choice of stellar feedback model had significant implications for the properties and evolution of the CGM. First of all, the metallicity distribution was strongly dependent on the ejective capabilities of the code implementation and stellar feedback, where more ejective, strongest for the AMR codes, resulted in a more metal-rich CGM. Continuing on the ejective efficiency, their differences were made even more clear from their respective closure radii R_c. Most predicted $R_c \sim R_{vir}$, meaning nearly all baryons were kept bound in the galaxy, while some, the AMR codes and AREPO-T, showed a significant loss of baryons, constituting to the "missing baryons problem". Regardless, most baryons predicted $\sim 20 - 50\%$ of their expected baryons were contained within their CGM, and by their final snapshot the majority of these baryons were contained within the hot ($T > 3 \cdot 10^5$ K) component, as expected. The evolution of the multiphase differed quite substantially, however, with the exception of the warm phase that for most codes fluctuated around $\sim 10\%$. From these dissimilarities, the difference between ejective and preventive feedback could be ascertained. The code with the strongest preventive feedback could establish a hot gas dominated CGM already by $z \sim 4$, while the strongest ejective model in ART-I instead was not hot gas dominated until $z \lesssim 1.2$. The virialisation condition $t_{cool}/t_{ff} \approx 1$ further strengthened these differences, and again the ejective models showed a much later inner CGM virialisation than the other models. But, surprisingly, these results did not manage to reproduce the expected inside-out or outside-in virialisation, except for the exceptionally ejective code ART-I that predicted outside-in virialisation. Instead, this work predicts a third alternative of instead halo wide virialisation at the same epoch, although which epoch was slightly different between codes. For the majority of codes, however, the difference between the redshift that this virialisation occurred decreased with radial distance, with $z \sim 2.5 \pm 0.2$ at 150 kpc and 2.6 ± 0.3 at 200 kpc. These results show that the CGM is assuredly a suitable region for studying differences depending on the chosen both numerical implementation and stellar feedback model.

The simulations used in this work were focused on only comparing and distinguishing differences based on stellar feedback models and numerical implementation, but each code were restricted to only one model each. In the future, the AGORA Collaboration aim to modify these simulations and not only vary the stellar feedback model, testing multiple parameters per code, but also eventually include even more physical processes, such as magnetic fields and cosmic rays. In addition, it is known that resolution can also cause discrepancies and thus it is also an ongoing effort of the AGORA Collaboration to investigate differences determined by resolution as well. Finally, the power of code comparison project is not only rooted in how well the differences can be distinguished, but also simply the amount of codes that are being compared. One of the many goals of the AGORA Collaboration is to also include more and more simulation codes, with their respective code groups, increasing the predictive power and ability to differentiate between simulations using different numerical implementation.

Chapter 6

Contribution

This section clarifies which aspects of this project were conducted entirely by the student and which were done by other persons.

- All parts, not including the paper, were entirely written by the student, with edit suggestions by the examiner Ross Church. Any figures not made by the student in this thesis have been properly cited.
- The paper:
  - The abstract was mostly written by the main supervisor Oscar Agertz.
  - The introduction was written primarily by the student, although heavily edited by Oscar Agertz, and suggestions for edits were provided by Víctor Rufo-Pastor.
  - The method section was written almost entirely by the student, with mild comments from Oscar Agertz and Víctor Rufo-Pastor.
  - All of the results and discussion were written by the student, although with significant comments and corrections from the co-supervisor Santi Roca-Fàbrega.
  - The conclusion section was written by the student, with suggestions from Oscar Agertz.

Bibliography

Agertz O., et al., 2007, MNRAS, 380, 963

Anand A., Nelson D., Kauffmann G., 2021, MNRAS, 504, 65–88

Aoyama S., Hou K.-C., Shimizu I., Hirashita H., Todoroki K., Choi J.-H., Nagamine K., 2016, MNRAS, 466, 105

Berger M., Colella P., 1989, Journal of Computational Physics, 82, 64

Birnboim Y., Dekel A., 2003, MNRAS, 345, 349

Bryan G. L., Norman M. L., 1998, ApJ, 495, 80

Bryan G. L., et al., 2014, ApJS, 211, 19

Carfora M., Familiari F., 2026, General Relativity and Gravitation, 58, 7

Ceverino D., Primack J., Dekel A., Kassin S. A., 2017, MNRAS, 467, 2664

Ceverino D., Mandelker N., Snyder G. F., Lapiner S., Dekel A., Primack J., Ginzburg O., Larkin S., 2023, MNRAS, 522, 3912

Chabrier G., 2003, ApJ, 586, L133

Chen H.-W., Zahedy F. S., 2026, in , Encyclopedia of Astrophysics. Elsevier, pp 370–400, doi:10.1016/B978-0-443-21439-4.00059-6

Cirelli M., Strumia A., Zupan J., 2024, Dark Matter (arXiv:2406.01705)

Davis M., Efstathiou G., Frenk C. S., White S. D. M., 1985, ApJ, 292, 371

Dehnen W., Aly H., 2012, MNRAS, 425, 1068

Dekel A., Birnboim Y., 2006, MNRAS, 368, 2

Durier F., Dalla Vecchia C., 2012, MNRAS, 419, 465

Efstathiou G., Davis M., White S. D. M., Frenk C. S., 1985, ApJS, 57, 241

Faerman Y., Pandya V., Somerville R. S., Sternberg A., 2022, ApJ, 928, 37

Faucher-Giguère C.-A., Oh S. P., 2023, ARA&A, 61, 131

Ferland G. J., et al., 2013, Rev. Mex. Astron. Astrofis., 49, 137

Fielding D., Quataert E., McCourt M., Thompson T. A., 2017, MNRAS, 466, 3810

Frenk C. S., et al., 1999, ApJ, 525, 554

Gronke M., E. Schneider E., 2026, Living Reviews in Computational Astrophysics, 12, 2

Hahn O., Abel T., 2011, MNRAS, 415, 2101

Hopkins P. F., 2013, MNRAS, 428, 2840

Hopkins P. F., 2015, MNRAS, 450, 53

Hopkins P. F., et al., 2018, MNRAS, 480, 800

Hubble E. P., 1925, The Observatory, 48, 139

Jung M., et al., 2025, ApJ, 994, 245

Keller B. W., Wadsley J., Benincasa S. M., Couchman H. M. P., 2014, MNRAS, 442, 3013

Khouri, T. et al., 2026, A&A, 707, A162

Kim J.-h., et al., 2014, ApJS, 210, 14

Kim J.-h., et al., 2016, ApJ, 833, 202

Klypin A., Gottlöber S., Kravtsov A. V., Khokhlov A. M., 1999, ApJ, 516, 530

Kobayashi C., Tsujimoto T., Nomoto K., 2000, ApJ, 539, 26

Kravtsov A. V., Klypin A. A., Khokhlov A. M., 1997, ApJS, 111, 73

Kravtsov A. V., Vikhlinin A. A., Meshcheryakov A. V., 2018, Astronomy Letters, 44, 8

Long A. S., et al., 2024, ApJ, 970, 68

Lupi A., Pallottini A., Ferrara A., Bovino S., Carniani S., Vallini L., 2020, MNRAS, 496, 5160

Matteucci F., Greggio L., 1986, A&A, 154, 279

McClain R. L., Mathur S., Das S., Krongold Y., Gupta A., 2024, MNRAS, 527, 5093

Menon H., Wesolowski L., Zheng G., Jetley P., Kale L., Quinn T., Governato F., 2015, Computational Astrophysics and Cosmology, 2, 1

Mo H., van den Bosch F. C., White S., 2010, Galaxy Formation and Evolution, doi:10.1017/CBO9780511807244.

Morris J. P., 1996, Publ. Astron. Soc. Australia, 13, 97

Münch G., Zirin H., 1961, ApJ, 133, 11

NASA/LAMBDA-Science-Team 2016, LCDM Model of Cosmology, `https://lambda.gsfc.nasa.gov/education/graphic_history/univ_evol.html`

Naab T., Ostriker J. P., 2017, ARA&A, 55, 59

Ng Y. V., et al., 2025, ApJ, 993, 92

O'Shea B. W., Nagamine K., Springel V., Hernquist L., Norman M. L., 2005, ApJS, 160, 1

Oh B. K., Smith B. D., Peacock J. A., Khochfar S., 2020, MNRAS, 497, 5203

Peeples M. S., Werk J. K., Tumlinson J., Oppenheimer B. D., Prochaska J. X., Katz N., Weinberg D. H., 2014, ApJ, 786, 54

Peng B., et al., 2025, A&A, 694, L1

Peroux C., Nelson D., 2024, The Multi-Scale Multi-Phase Circumgalactic Medium: Observed and Simulated (arXiv:2411.07988)

Planck Collaboration et al., 2020, A&A, 641, A6

Prochaska J. X., et al., 2017, ApJ, 837, 169

Putman M. E., Peek J. E. G., Joung M. R., 2012, ARA&A, 50, 491

Qu Z., Bregman J. N., 2019, ApJ, 880, 89

Raiteri C. M., Villata M., Navarro J. F., 1996, A&A, 315, 105

Rauch M., 1998, ARA&A, 36, 267

Revaz Y., Jablonka P., 2012, A&A, 538, A82

Revaz Y., Arnaudon A., Nichols M., Bonvin V., Jablonka P., 2016, A&A, 588, A21

Roca-Fàbrega S., et al., 2021, ApJ, 917, 64

Roca-Fàbrega S., et al., 2024, ApJ, 968, 125

Roca-Fàbrega S., et al., 2024, The AGORA high-resolution galaxy simulations comparison project: CosmoRun data release (arXiv:2408.00432)

Rodríguez-Puebla A., Primack J. R., Avila-Reese V., Faber S. M., 2017, MNRAS, 470, 651

Saitoh T. R., 2017, AJ, 153, 85

Saitoh T. R., Makino J., 2009, ApJ, 697, L99

Saitoh T. R., Makino J., 2013, ApJ, 768, 44

Scalzo R. A., Ruiter A. J., Sim S. A., 2014, MNRAS, 445, 2535

Scannapieco C., et al., 2012, MNRAS, 423, 1726

Shen S., Wadsley J., Stinson G., 2010, MNRAS, 407, 1581

Shen S., Madau P., Guedes J., Mayer L., Prochaska J. X., Wadsley J., 2013, ApJ, 765, 89

Shimizu I., Todoroki K., Yajima H., Nagamine K., 2019, MNRAS, 484, 2632

Smith B. D., et al., 2017, MNRAS, 466, 2217

Spitzer Jr. L., 1956, ApJ, 124, 20

Springel V., 2010, MNRAS, 401, 791–851

Springel V., Yoshida N., White S. D. M., 2001, New Astron., 6, 79

Springel V., et al., 2005, Nature, 435, 629

Stern J., Hennawi J. F., Prochaska J. X., Werk J. K., 2016, ApJ, 830, 87

Stern J., Fielding D., Faucher-Giguère C.-A., Quataert E., 2019, MNRAS, 488, 2549

Stern J., Fielding D., Faucher-Giguère C.-A., Quataert E., 2020, MNRAS, 492, 6042

Stinson G., Seth A., Katz N., Wadsley J., Governato F., Quinn T., 2006, MNRAS, 373, 1074

Strawn C., et al., 2024, ApJ, 962, 29

Suresh J., Bird S., Vogelsberger M., Genel S., Torrey P., Sijacki D., Springel V., Hernquist L., 2015, MNRAS, 448, 895–909

Tolman R. C., 1930, Proceedings of the National Academy of Sciences, 16, 511

Tolman R. C., 1934, Relativity, Thermodynamics, and Cosmology. Oxford: Oxford University Press

Tsujimoto T., Nomoto K., Yoshii Y., Hashimoto M., Yanagida S., Thielemann F.-K., 1995, MNRAS, 277, 945

Tumlinson J., et al., 2011, Science, 334, 948

Tumlinson J., Peeples M. S., Werk J. K., 2017, ARA&A, 55, 389

Turk M. J., 2013, How to Scale a Code in the Human Dimension (`arXiv:1301.7064`)

Turk M. J., Smith B. D., 2011, High-Performance Astrophysical Simulations and Analysis with Python (`arXiv:1112.4482`)

Turk M. J., Smith B. D., Oishi J. S., Skory S., Skillman S. W., Abel T., Norman M. L., 2011, ApJS, 192, 9

Vogelsberger M., Marinacci F., Torrey P., Puchwein E., 2020, Nature Reviews Physics, 2, 42

Wadsley J. W., Keller B. W., Quinn T. R., 2017, MNRAS, 471, 2357

Werk J. K., et al., 2014, ApJ, 792, 8

Werk J. K., et al., 2016, ApJ, 833, 54

Wolfe A. M., Gawiser E., Prochaska J. X., 2005, ARA&A, 43, 861

Wright R. J., Somerville R. S., Lagos C. d. P., Schaller M., Davé R., Anglés-Alcázar D., Genel S., 2024, MNRAS, 532, 3417

Zhang Y., et al., 2024a, A&A, 690, A267

Zhang H., Li M., Zaritsky D., 2024b, ApJ, 974, 148

Zhang Y., et al., 2026, A&A, 706, A102

Zhu G., Ménard B., 2013, ApJ, 773, 16

van de Voort F., Schaye J., 2013, MNRAS, 430, 2688

van der Kruit P. C., Freeman K. C., 2011, ARA&A, 49, 301